Differential diffusion modelling for LES of premixed and partially premixed flames with presumed FDF

Ferrante, Gioele; Eitelberg, Georg; Langella, Ivan

DOI
10.1080/13647830.2024.2389099

Publication date
2024

Document Version
Final published version

Published in
Combustion Theory and Modelling

Citation (APA)
Ferrante, G., Eitelberg, G., & Langella, I. (2024). Differential diffusion modelling for LES of premixed and partially premixed flames with presumed FDF. *Combustion Theory and Modelling*, *28*(6), 695-730. https://doi.org/10.1080/13647830.2024.2389099

Important note
To cite this publication, please use the final published version (if applicable).
Please check the document version above.

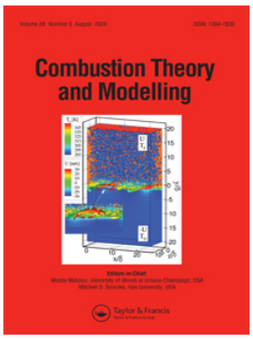

Taylor & Francis
Taylor & Francis Group

Combustion Theory and Modelling

ISSN: (Print) (Online) Journal homepage: www.tandfonline.com/journals/tctm20

Differential diffusion modelling for LES of premixed and partially premixed flames with presumed FDF

Gioele Ferrante, Georg Eitelberg & Ivan Langella

To cite this article: Gioele Ferrante, Georg Eitelberg & Ivan Langella (20 Aug 2024): Differential diffusion modelling for LES of premixed and partially premixed flames with presumed FDF, Combustion Theory and Modelling, DOI: 10.1080/13647830.2024.2389099

To link to this article: https://doi.org/10.1080/13647830.2024.2389099

Published online: 20 Aug 2024.

Combustion Theory and Modelling, 2024
https://doi.org/10.1080/13647830.2024.2389099

Differential diffusion modelling for LES of premixed and partially premixed flames with presumed FDF

Gioele Ferrante*, Georg Eitelberg and Ivan Langella

Faculty of Aerospace Engineering, Delft University of Technology, Delft, Netherlands

(*Received 8 February 2024; accepted 14 July 2024*)

Large eddy simulations (LES) with flamelet and presumed filtered density function closure are used to simulate turbulent premixed and partially premixed hydrogen flames. Different approaches to model differential diffusion are investigated and compared. In particular, two existing models are extended to the LES framework to correct the resolved diffusive flux of the controlling variables due to differential diffusion. A lean premixed turbulent hydrogen flame in a slotted burner configuration is simulated first to compare the capability of the considered models in capturing local mixture fraction redistribution, super-adiabatic temperatures and thermo-diffusive instabilities. Results show that both models describe the formation of cellular burning structures. Next, a partially premixed lifted hydrogen flame in vitiated hot coflow is simulated to gain insight on the relevance of differential diffusion modelling at a higher turbulence level, a different combustion mode and in the presence of a complex stabilisation mechanism. Good predictions of the turbulent mixing and temperature fields are observed. Moreover, results show that the flame lift-off height has an appreciable sensitivity to the differential diffusion model. When differential diffusion is included only in the thermochemistry database, only mild effects on the predicted temperature fields, mixing and flame height are observed. On the contrary, a considerable shift of the flame base is observed when corrections are applied in the LES at the resolved level, depending on what controlling variables are considered. Further analyses reveal how the corrections of diffusive fluxes in the thermochemistry and at the LES level affect differently the flame burning mode, whose details are given throughout the paper.

Keywords: Differential diffusion; hydrogen; LES; flamelet/presumed FDF

1. Introduction

Hydrogen is a promising alternative energy carrier for power generation systems due to its carbon-free combustion and to the possibility of producing it via water electrolysis using renewable energy [1]. Its high specific energy opens broad possibilities in applications where high power is of utmost importance, for example in the aeronautical sector. Moreover, the wide flammability range of hydrogen can be exploited to stabilise the flame at premixed ultra-lean conditions with a reduction of the flame temperature. This can be exploited to suppress the NOx formation, which is exponentially dependent on temperature due to Zel'dovich mechanism [2]. On the other hand, the relatively short auto-ignition

*Corresponding author. Email: g.ferrante@tudelft.nl

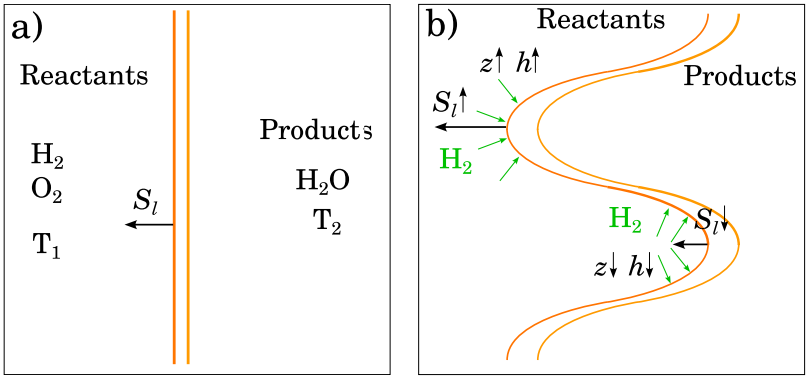

Figure 1. Sketch of a laminar premixed freely propagating hydrogen/air flame. (a) Flat flame and (b) Curved flame, showing the coupling between flame front curvature and differential diffusion.

delay time, strong reactivity and flame speed of hydrogen exacerbate the risk of flashback and instabilities, requiring specific flame holder designs to ensure stabilisation [3]. Additional challenges arise from the fact that the molecular diffusivity of hydrogen is higher than the thermal diffusivity and the molecular diffusivity of the other species, which results in a local redistribution of equivalence ratio ϕ and enthalpy h across the flame front. This effect can be observed for example for a flat and unstretched 1D laminar freely propagating premixed hydrogen-oxygen flame sketched in Figure 1(a). Here, enthalpy and Bilger's mixture fraction z [4] are conserved between reactants and products, but they vary across the flame front [5, 6]. For a premixed flame propagating in space the fast molecular diffusion of the deficient reactant further couples with the flame front curvature, as sketched in Figure 1(b). When the Lewis number of the fuel in the reactants' mixture falls below a critical value, the imbalance between the species mass diffusion towards the flame and heat diffusion fluxes towards the reactants in the preheat zone causes inhomogeneous variations in mixture fraction, enthalpy and consequently consumption speed [7–9], which can lead to thermo-diffusive instabilities [9, 10], with significant increase of flame surface [11–13]. These processes need to be thoroughly understood in order to achieve full control of hydrogen flames.

The development of accurate numerical predictive tools is of high interest for the analysis and understanding of complex behaviours in turbulent reacting flows such as those described above. In this context, large eddy simulation (LES) is very attractive due to the possibility of predicting unsteady flow features at an affordable computational cost [14]. In a LES, the large turbulent flow structures are time-resolved, while the subgrid scales (SGS) falling below the LES filter size are modelled. Many LES combustion models have been developed for premixed and partially premixed flames to account for the subgrid turbulence-chemistry interaction, and extensive reviews can be found in literature, e.g. see [15, 16]. Among these, flamelets approaches have been broadly used in combustion due to their relatively low computational cost, robustness and versatility [17–19]. Flamelet models rely on the assumption that a turbulent flame can be represented as an ensemble of locally 1D laminar flamelets. This way, turbulence can be separated from thermochemistry, and the latter can be computed *a priori* using 1D laminar solutions (flamelets). Within this category, the effect of turbulence on flame wrinkling is typically taken into account statistically using a presumed filtered density function (FDF) [15, 16, 20, 21]. These methods

have been widely employed for the prediction of hydrocarbon flames, providing very satisfactory results at various conditions (e.g. see [21, 22]). However, they often rely on the assumption of equi-diffusivity of species and heat, which does not hold in problems involving non-unity Lewis number fuels, such as hydrogen. Indeed, in LES analysis of practical turbulent hydrogen flames, flamelet models have been often employed neglecting differential diffusion effects, under the assumption that turbulent transport dominates over molecular diffusive phenomena [23, 24]. However, it is unclear whether this assumption holds. In [9] the reactants' diffusivity was shown to have a substantial effect on the turbulent flame speed. The formation of bulges, cellular burning structures and reaction rate inhomogeneities in hydrogen-air premixed flames subject to moderate turbulence was observed both experimentally and numerically in various studies [13]. Berger et al. [25], using direct numerical simulations (DNS), described the synergistic interplay between differential diffusion effects and turbulence-induced curvature and strain. Similarly, Rieth et al. [26] identified the coupling between hydrogen differential diffusion and flame front curvature as a dominant process on the consumption rate distribution also at high Karlovitz number, which was observed to be even amplified at high pressure conditions [27]. These effects typically originate at smaller scales than the LES filter size and cause flame self-wrinkling, increase in flame surface and inhomogenous variation of reaction rate. Common flamelets-based models are unable to capture these effects since the mixture fraction is a conserved scalar only describing fuel-oxidiser mixing, and the same diffusion coefficient is used for all the controlling variables. Modifications to the flamelet models have been proposed in the context of DNS to account for differential diffusion without resorting to fully transported chemistry. In [5] a correction to the mixture fraction transport equation is applied by means of a source term. This approach appeared to be capable of correctly capturing the local redistribution of mixture fraction due to differential diffusion, and also the formation of thermo-diffusive instabilities. Van Oijen and coworkers [28–30] proposed another approach where a similar correction to the diffusive term in the transport equations of mixture fraction is applied, along with further corrections in the diffusive fluxes of progress variable and enthalpy. As compared to the approach in [5], the latter allows to model also the redistribution of enthalpy due to differential diffusion, useful in problems involving stream mixing and heat losses.

The aforementioned approaches have been proven to be very effective in mimicking the effects of differential diffusion when employed in DNS of premixed flames with tabulated chemistry, but their application in flamelets models in the context of turbulent LES has been so far limited [31, 32]. In this case differential diffusion occurs typically at the subgrid level and different considerations apply depending on the ratio between the LES filter width Δ and the local flame thickness δ. For $\Delta/\delta \to 0$ (flame front resolved, DNS limit), the correct prediction of the redistribution of equivalence ratio and enthalpy across the flame is sufficient to predict the correct surface growth due to eventual thermo-diffusive instabilities, as demonstrated in [5]. One can expect that as the flame front becomes more and more unresolved, one also has to mimic the subgrid flame surface growth due to the instabilities in order to predict the correct turbulent flame speed in a certain cell of the domain. While different approaches have been proposed for the prediction of the surface growth (e.g. see [11]), this modelling is beyond the purposes of the present study and is therefore not discussed further here. In the assumption that the flame front is partially resolved ($\Delta/\delta \approx 1$ or less, but above the DNS limit), it is important to make another distinction. For a premixed flat flame Figure 1(a), assuming negligible gradients in the flame tangential direction, all thermochemical states are associated with the same flamelet (where

differential diffusion is taken into account). Any variation at the resolved level in the LES due to differential diffusion in progress variable, mixture fraction and enthalpy must be consistent with that observable in the flamelet and these variables are not independent. The correct thermochemical state can in this case be retrieved by using just the progress variable, with the correct diffusion coefficient at the resolved level. The situation is more complex when the flame front is curved, which might occur due to self-induced perturbations or turbulence Figure 1(b). In this case the coupling between differential diffusion and curvature causes additional variations in the mixture composition and enthalpy in the preheat region and across the flame due to converging (diverging) effect on the diffusion transport fluxes. This leads to thermochemical states which are not representable by a single flamelet, since the composition of reactants upstream of the flame is modified by the curvature itself. An extension of the chemical database to a collection of flamelets at different reactant compositions is thus necessary. It is therefore critical in this second case to accurately assign the right corrections in the diffusion fluxes of the controlling variables in order to capture this coupling phenomena and access the correct thermochemical state in the flamelets database. In the context of presumed FDF approaches, however, additional unclosed terms would appear in the corrective diffusion terms of the controlling variables, and how to model these terms is not fully clear.

In the present work, the aim is to shed light on the aforementioned uncertainties in the modelling of differential diffusion in the context of flamelet-based LES with presumed FDF closure. A baseline model used and validated for hydrocarbon flames in a broad range of conditions [33–35] is extended with the objective to understand the relative importance of modelling differential diffusion by accounting for it at the thermochemistry level and at the resolved scales in a LES. To this purpose differential diffusion is first included only in the thermochemical database and the effects of the database variations on the LES results are assessed. In a second step, the two models introduced earlier [5, 30] are extended to the present flamelet/presumed FDF framework in order to include differential diffusion also at the resolved scales, and different possible implementations are assessed and compared. Two test cases are selected to assess the capabilities of the aforementioned models at different turbulence and combustion mode conditions. The turbulent premixed hydrogen flame studied by Berger et al. [25] is simulated first. Being a premixed case, mixture fraction variations are only caused by differential diffusion effects. Therefore, this case offers a good benchmark to assess the effectiveness of the proposed models in describing the local mixture fraction redistribution, its coupling with flame front curvature and the occurrence of super-adiabatic temperatures. The second case analysed is the partially premixed lifted hydrogen flame in vitiated coflow studied by Cabra et al. [36, 37]. In this flame, mixture fraction variations are already present due to fuel-oxidiser mixing, which controls the flame stabilisation, and the effects of differential diffusion on this stabilisation mechanism are investigated. The Cabra flame has been widely studied at different fuel compositions and operating conditions both experimentally [38, 39] and numerically [40, 41]. In [42] differential diffusion effects were studied by means of transported FDF model with detailed chemistry and shown to be still relevant in the presence of turbulence. In [43] a flamelet approach including premixed, non-premixed and autoignition modes was successfully employed for the prediction of the lifted flame. Premixed flamelets models have also been recently used [23, 24], however neglecting differential diffusion effects. The present study investigates various strategies to include differential diffusion modelling in the flamelet/presumed FDF LES simulation of this partially premixed test case, analysing their effects on the flame

structure and stabilisation. This paper is organised as follows. First the two test cases are described in Section 2. In Section 3 the flamelet/presumed FDF methodology is introduced, together with the description of the differential diffusion models. Numerical details are provided in Section 4. In Section 5 the LES results are analysed to understand the effects of differential diffusion modelling for the two test cases. Final remarks are provided in Section 6.

2. Test cases

Two test cases are studied in the present work. The first case is the turbulent lean premixed hydrogen-air flame in slot burner configuration studied in [25] by means of DNS, which is simulated here to gain insight into the capabilities of the LES to capture relevant effects of differential diffusion on the flame topology. A hydrogen/air mixture at an equivalence ratio of $\phi = 0.4$ and temperature $T_{\text{reac}} = 300\,\text{K}$ is issued at a bulk velocity $U_{\text{bulk}} = 24\,\text{m/s}$ into a secondary stream composed by the combustion products at temperature $T_{\text{prod}} = 1425\,\text{K}$ and velocity $U_{\text{prod}} = 3.5\,\text{m/s}$, see Figure 2(c). The jet Reynolds number based on the nozzle width $H = 8\,\text{mm}$ is $\text{Re} = 11000$. Berger et al. [25] observed that when an equidiffusive assumption was used, the flame speed was only affected by turbulence, while flame self-wrinkling and local variations of flame temperature and reaction rate were observed in the more realistic case with differential diffusion. This second case resulted in an increased turbulent flame speed and an overall shorter flame. Therefore, this test case represents a good benchmark for the assessment of the effectiveness of the differential diffusion models in the LES. Only the thermo-diffusively unstable case is simulated in the present study. Table 1 reports the operating conditions of the case, including reactants and product compositions in terms of species mole fractions X_i.

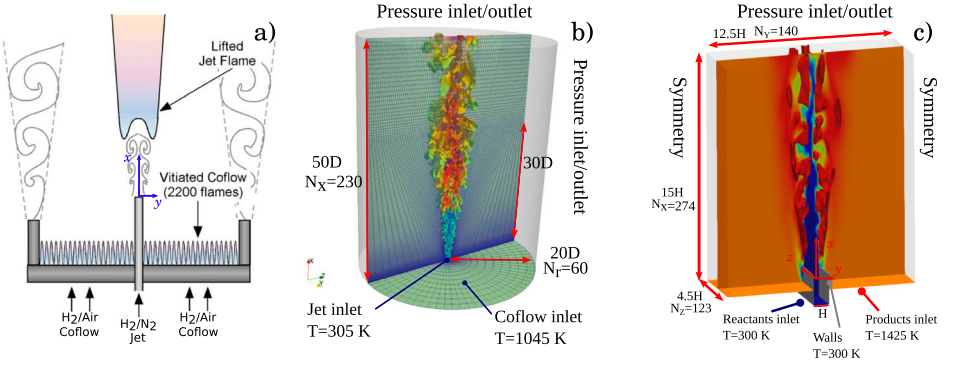

Figure 2. Sketch of the lifted flame burner [36] (left), lifted flame computational domain (center), slotted burner computational domain (right).

Table 1. Operating conditions for the premixed hydrogen slot burner case.

	U_{bulk} [m/s]	Re	T [K]	X_{H_2}	X_{O_2}	X_{N_2}	X_{H_2O}
Reactants stream	24	11,000	300	0.0116	0.2296	0.7588	0.0
Products stream	3.5	–	1425	–	0.1376	0.7588	0.1036

Table 2. Operating conditions of the lifted partially premixed hydrogen flame case.

	D [mm]	U_{bulk} [m/s]	Re	T [K]	X_{H_2}	X_{O_2}	X_{N_2}	X_{H_2O}
Jet	4.57	107	23,600	305	0.25	–	0.75	–
Coflow	210	3.5	18,600	1045	–	0.1474	0.7534	0.0989

The second case is the partially premixed lifted hydrogen flame in hot coflow studied experimentally by Cabra et al. [36]. The setup, sketched in Figure 2(a), consists of a central nozzle with an inner diameter D of 4.57 mm and an outer diameter of 6.35 mm, issuing a fuel mixture composed of 25% H_2 and 75% N_2 in volume. The bulk velocity of the fuel stream is 107 m/s. The hot coflow is at a temperature of 1045 K and is composed by the products (H_2O, O_2 and N_2) of a lean H_2/air flame at equivalence ratio $\phi = 0.25$. In [36] the mixture fraction z is defined according to Bilger's formulation [4], resulting in a value at stoichiometry of $z_{\text{st}} = 0.4741$. The flames producing the hot coflow are stabilised on a perforated plate with a diameter of 210 mm located 70 mm upstream of the central nozzle exit. The plate is confined by a collar, in order to prevent the entrainment of external air to interfere with the flame region. This way, the central jet is surrounded by a homogeneous coflow of known temperature and composition. Measurements using Raman-Rayleigh scattering and laser-induced fluorescence were taken on the centreline from 0 to 26 nozzle diameters downstream. Radial profiles were measured at streamwise locations from 8D to 26D. Wu et al. [39] further characterised the turbulent flow field under different operating conditions for both reacting and non reacting cases. Laser doppler velocimetry (LDV) was used to provide measurements of average axial velocity, axial and radial velocity rms and Reynolds shear stress. This burner is simulated here using LES paradigms under the operating conditions described in [36] and reported in Table 2.

3. Methodology

A flamelet-based approach with presumed FDF, already validated for hydrocarbon flames [34, 44–46] is used to model the turbulence-flame interaction in the LES. The baseline model with equal diffusivities is described first in Section 3.1, and variations to this modelling to incorporate differential diffusion effects are discussed in Section 3.2.

3.1. *Combustion modelling*

Flamelet-based models rely on the assumption that the smallest turbulent eddies can stretch and wrinkle the flame front but are not able to affect the inner flame structure. All the thermochemical states of the reacting mixture can therefore be described by a set of 1D laminar flamelets using a limited number of controllling variables, which largely reduces the number of transported scalars in the LES [47]. This assumption is valid in a broad range of conditions and allows good predictions as described in [21, 48]. In the present work the chemical database is built on a set of unstrained 1D premixed flamelets parameterised on a progress variable c and spanning the flammability range for different values of mixture fraction z. The mixture fraction is defined according to Bilger's definition [4] as

$$z = \frac{0.5W_{H_2}(z_H - z_{H,2}) - W_{O_2}^{-1}(z_O - z_{O,2})}{0.5W_{H_2}(z_{H,1} - z_{H,2}) - W_{O_2}^{-1}(z_{O,1} - z_{O,2})}, \tag{1}$$

where subscripts 1 and 2 indicate respectively fuel and the oxydiser streams, z_H and z_O are the hydrogen and oxygen elemental mass fractions, and W_i refers to the molar mass of species i. The progress variable is defined as the variation in water mass fraction with respect to its value in the reactants stream, in line with previous studies [21, 49]. Its value is scaled here to be bounded between 0 and 1 as follows:

$$c = \frac{\Delta Y_{\mathrm{H_2O}}(z)}{\psi_{\max}(z)} = \frac{Y_{\mathrm{H_2O}}(z) - Y^{\mathrm{reac}}_{\mathrm{H_2O}}(z)}{Y^{\mathrm{prod}}_{\mathrm{H_2O}}(z) - Y^{\mathrm{reac}}_{\mathrm{H_2O}}(z)}, \tag{2}$$

were the superscripts 'reac' and 'prod' refer to reactants and products respectively. When differential diffusion is not taken into account and unity Lewis number is assumed for every species, the Favre-filtered mixture fraction $\widetilde{z}$ is a passive scalar describing the fuel and oxidiser streams mixing and its transport equation is:

$$\overline{\rho}\frac{D\widetilde{z}}{Dt} = \nabla \cdot \left[\left(\overline{\rho\mathcal{D}} + \frac{\mu_t}{\mathrm{Sc}_t}\right)\nabla\widetilde{z}\right], \tag{3}$$

in which D/Dt represents the material derivative, the mixture density is indicated with ρ and the filtered molecular mass diffusion coefficient is defined as $\overline{\rho\mathcal{D}} = \widetilde{\mu}/\mathrm{Sc}$, where Sc is the laminar Schmidt number. The filtered dynamic viscosity μ is calculated via Sutherland's law. The SGS viscosity, μ_t, is defined by the turbulence model, and $\mathrm{Sc}_t = 0.4$ is the turbulent Schmidt number. The transport equation for the filtered progress variable $\widetilde{c}$ is:

$$\overline{\rho}\frac{D\widetilde{c}}{Dt} = \nabla \cdot \left[\left(\overline{\rho\mathcal{D}} + \frac{\mu_t}{Sc_t}\right)\nabla\widetilde{c}\right] + \overline{\dot{\omega}}_c. \tag{4}$$

The filtered reaction rate $\overline{\dot{\omega}}_c$ in the above equation is expressed as [34, 50]

$$\overline{\dot{\omega}_c}(\tilde{c}, \tilde{z}, \sigma_c^2, \sigma_z^2) = \overline{\rho}\int_0^1\int_0^1 \frac{\dot{\omega}_c(c,z)}{\rho(c,z)} P(c,z;\tilde{c},\tilde{z},\sigma_c^2,\sigma_z^2)\,\mathrm{d}c\,\mathrm{d}z + \overline{\dot{\omega}}_{\mathrm{np}}. \tag{5}$$

where the progress variable reaction rate $\dot{\omega}_c(c,z) = \dot{\omega}_{\mathrm{H_2O}}(c,z)/\psi_{\max}(z)$ within the integral is taken from 1D laminar flamelets computation. The term $\overline{\dot{\omega}}_{\mathrm{np}}$ results from the use of a scaled progress variable and the dependence of the scaling factor $\psi_{\max}(z)$ on the mixture fraction. It represents a correction due to non-premixed mode and is defined as [35]:

$$\overline{\dot{\omega}}_{\mathrm{np}}(\tilde{z},\sigma_z^2) = \overline{\rho}\widetilde{c}\widetilde{\chi}_z \int_0^1 \frac{1}{\psi_{\max}(z)}\frac{d^2\psi_{\max}(z)}{d\,z^2} P(z;\tilde{z},\sigma_z^2)\,\mathrm{d}z. \tag{6}$$

where $\widetilde{\chi}_z = \widetilde{D}\nabla\widetilde{z}\cdot\nabla\widetilde{z} + \widetilde{\varepsilon}_z$ is the sum of resolved and SGS scalar dissipation rate (SDR) of mixture fraction, and the subgrid part is modelled using linear relaxation as $\widetilde{\varepsilon}_z = c_z(\nu_t/\Delta^2)\sigma_z^2$, with $c_z \approx 2$ [15] and $\Delta = \mathcal{V}^{1/3}$, $\mathcal{V}$ being the volume of the local cell in the computational mesh. A Beta distribution is chosen to describe the joint FDF $P(c,z)$ following previous studies [19, 21] and given the good performance observed in regimes similar to those investigated in the present study [34, 51]. Under the assumption of statistical independence between the controlling variables the joint FDF is then expressed as the product of two distinct FDFs [16], which was shown to be reasonable for well resolved LES [52].

The shape of the Beta distribution depends on the filtered value ($\widetilde{c}$ or $\widetilde{z}$) and its subgrid variance (σ_c^2 or σ_z^2). The SGS variances are computed by solving their transport equations. For the subgrid variance of progress variable this equation reads:

$$\overline{\rho}\frac{D\widetilde{\sigma_c^2}}{Dt} = \nabla\cdot\left[\left(\overline{\rho\mathcal{D}}+\frac{\mu_t}{\mathrm{Sc}_t}\right)\nabla\widetilde{\sigma^2}_c\right] - 2\overline{\rho}\widetilde{\varepsilon}_c + 2\frac{\mu_t}{\mathrm{Sc}_t}(\nabla\widetilde{c}\cdot\nabla\widetilde{c}) + 2(\overline{c\dot{\omega}_c}-\widetilde{c}\overline{\dot{\omega}_c}), \tag{7}$$

where the source term $\overline{c\dot{\omega}}$ is computed consistently to Equation (5) and tabulated. The modelling of the SGS scalar dissipation rate $\widetilde{\varepsilon}_c$ follows the approach proposed in [53] and the dynamic procedure presented in [54,55]. The transport equation for the mixture fraction SGS variance reads:

$$\overline{\rho}\frac{D\widetilde{\sigma_z^2}}{Dt} = \nabla\cdot\left[\left(\overline{\rho\mathcal{D}}+\frac{\mu_t}{\mathrm{Sc}_t}\right)\nabla\widetilde{\sigma^2}_z\right] - 2\overline{\rho}\widetilde{\varepsilon}_z + 2\frac{\mu_t}{\mathrm{Sc}_t}(\nabla\widetilde{z}\cdot\nabla\widetilde{z}), \tag{8}$$

Enthalpy is not used as an additional controlling variable, as often done in problems including heat losses [29], but its transport equation is still resolved to better capture multi stream mixing. Using a density-varying, low-Mach approximation, the transport equation for the filtered absolute enthalpy $\widetilde{h}$ (sum of formation and sensible enthalpy) can be expressed as

$$\overline{\rho}\frac{D\widetilde{h}}{Dt} = \nabla\cdot\left[\left(\overline{\rho\mathcal{D}}+\frac{\mu_t}{\mathrm{Pr}_t}\right)\nabla\widetilde{h}\right] \tag{9}$$

where the turbulent heat diffusivity is modelled as μ_t/Pr_t and $\mathrm{Pr}_t = 0.4$ is the SGS Prandtl number.

3.2. *Differential diffusion modelling*

The flamelet database is built from the 1D solution of the reacting Navier-Stokes equations [16] in premixed freely propagating flame configuration. In a multi-component mixture, the species diffusion velocities of species k, $\mathbf{v}_k$, are mainly driven by mole fraction gradients, ∇X_k, and can be computed through the Stefan-Maxwell system of equations [7], in which the binary diffusion coefficients between all the species appear. The problem's complexity can be reduced by defining a diffusion coefficient $\mathcal{D}_k^M$ of each species k with respect to the mixture M [57], such that:

$$\mathbf{v}_k = -\mathcal{D}_k^M\frac{\nabla X_k}{X_k}, \tag{10}$$

The diffusion coefficients are linked to the heat diffusivity of the mixture through the Lewis number of each species, $\mathcal{D}_k^M = \alpha/\mathrm{Le}_k$. The heat diffusivity can be defined through the thermal conductivity λ as $\alpha = \lambda/(\rho C_p)$, where C_p is the heat capacity at constant pressure of the mixture. The transport model is often further simplified assuming equal diffusivity of heat and species, i.e. $\mathrm{Le}_k = 1$. While being generally reasonable for hydrocarbon mixtures and widely employed in combustion models, this assumption is arguable for hydrogen, whose Lewis number is around 0.3 in mixtures with air. Therefore a mixture-averaged diffusion model [16, 58] is employed in this work when accounting for differential diffusion

in the flamelets database, where the diffusion coefficient is computed as:

$$\mathcal{D}_k^M = \frac{1 - Y_k}{\sum_{j,k\neq j}^{N} X_j/\mathcal{D}_{jk}}. \tag{11}$$

In the above, D_{jk} is the binary diffusion coefficient of species j in species k. Figure 3 reports the progress variable reaction rate values resulting form hydrogen/air flamelets in the progress variable and mixture fraction spaces, under the assumption of unity and non-unity species Lewis number. It can be observed that differential diffusion causes a shift of the reaction rate peak to richer conditions and an overall increase in the peak value. In the physical space the thickness of the computed flamelets is affected by the diffusion model, and reactions occur over a broader progress variable range when differential diffusion is taken into account ($\mathrm{Le}_k \neq 1$). Differential diffusion effects on 1D laminar flamelets can be further assessed by looking at Figure 4(a), showing the trend of mixture fraction along flamelets at different reactants equivalence ratios; and at Figure 4(b) reporting a comparison between the peak reaction rate values for different reactants mixture fractions for the cases with and without differential diffusion modelling. One can observe that z decreases across the flame, which in turns reduces the peak reaction rate for the lean flamelets and increases it for the rich ones, with a cross-over around $\phi = 0.96$. These effects are thus non-negligible and must be taken into account in the tabulated thermo-chemistry in order to cover all thermochemical states.

In the LES framework, a correction of the controlling variables' diffusive transport is also necessary to account for differential diffusion effects as local equivalence ratio redistribution and flame curvature are coupled at the resolved scales. Two models originally developed for DNS of laminar flames are extended here for a turbulent LES case in the context of presumed FDF closure. The first approach, proposed in [5], consists in deriving a correction for the mixture fraction transport equation only. This model assumes equal mass diffusivity for all species and heat $\mathcal{D}_k = \mathcal{D} = \alpha$, except for hydrogen, whose Lewis number is taken to be $\mathrm{Le}_{\mathrm{H}_2} = 0.3$. Starting from the exact definition of hydrogen and oxygen diffusive fluxes, a corrected diffusion flux for the mixture fraction is derived and included in the transport equation as follows:

$$\rho\frac{Dz}{Dt} = \nabla\cdot(\rho\mathcal{D}_z\nabla z) + \dot{\omega}_z, \tag{12}$$

where a modified diffusion coefficient $\mathcal{D}_z$ and a source term $\dot{\omega}_z$ appear. With respect to the definition in [5], the correction terms are here reformulated to be compatible with the use of a scaled progress variable:

$$\dot{\omega}_z = -\nabla\cdot\left[\rho\mathcal{D}\left(\frac{1}{s+1}\right)\left(\frac{1}{\mathrm{Le}_{\mathrm{H}_2}} - 1\right)(1-z)\nabla(c\psi_{\max})\right]. \tag{13}$$

where s is the oxygen to fuel stoichiometric mass ratio. It can be seen how this additional term acts as a source or sink across the flame front through its dependence on the gradient of c and it was observed to yield the correct local equivalence ratio redistribution across the resolved flame front [5]. The term $\mathcal{D}_z$ is defined as:

$$\mathcal{D}_z = \mathcal{D}\left[1 + \left(\frac{1}{\mathrm{Le}_{\mathrm{H}_2}} - 1\right)(1-z)\right]. \tag{14}$$

This expression ensures a correction in the diffusion coefficient also in non-reacting regions, thus accounting for the higher diffusivity of H_2 in mixing processes. Equation (12)

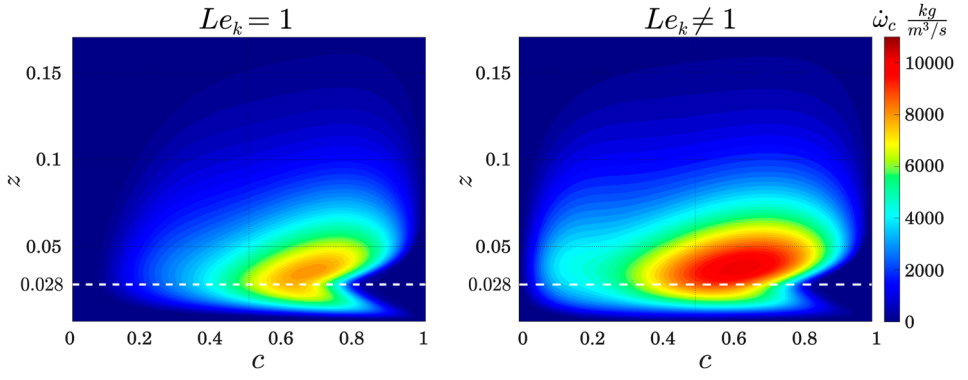

Figure 3. Contour plots of scaled progress variable reaction rate in the $c - z$ space for a hydrogen/air flame, reactants temperature $T_{\text{reac}} = 300\,\text{K}$, with unity Lewis number (left) and mixture averaged diffusion model (right). Results obtained using the kinetic mechanism of Burke et al. [56]. The stoichiometric condition $z_{\text{st}} = 0.028$ is marked with a white dashed line.

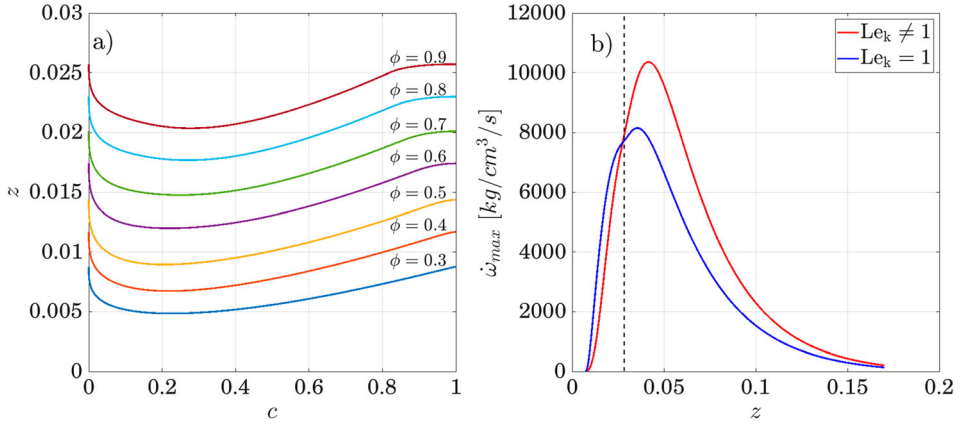

Figure 4. (a) Mixture fraction variation in progress variable space across a 1D freely propagating hydrogen/air flame at different reactants equivalence ratios and with reactants temperature $T_{\text{reac}} = 300\,\text{K}$. (b) Maximum reaction rate for different reactants mixture fraction values obtained with and without differential diffusion modelling. Results obtained using the kinetic mechanism of Burke et al. [56]. The stoichiometric condition $z_{\text{st}} = 0.028$ is marked as a vertical black dashed line.

must be Favre-filtered to be solved in the LES context, which is done in the present work as follows. The 'uncorrected' mass diffusivity $\mathcal{D}$, taken equal to the heat diffusivity, is pre-integrated and tabulated in a manner similar to Equation (5). Additional terms arise due to subgrid correlations, for example between the mixture fraction and the gradient of progress variable. Therefore two implementation strategies are here proposed and compared. In one case an approach similar to [59] is adopted, where the value of $\dot{\omega}_z(c, z)$ is obtained in the $c - z$ space within the laminar flamelets, by computing the differential operators appearing in Equation (13) as one dimentional derivatives. The term $\dot{\omega}_z(c, z)$ is thus pre-integrated consistently with Equation (5) to obtain the filtered mixture fraction source term $\widetilde{\dot{\omega}}_z$, and tabulated. The other approach consists of implementing Equation (13) directly in the LES transport equation. This implies neglecting the subgrid correlations and only considering resolved filtered quantities (e.g. $\tilde{z}$, $\nabla\tilde{c}$) for the calculation of $\widetilde{\dot{\omega}}_z$.

The second differential diffusion model considered in this work was proposed in [28] and more recently reformulated in [30]. This approach is based on the expression of the controlling variables as a linear combination of the species:

$$c = \sum_{i}^{N_s} \mathcal{C}_i Y_i$$
$$z = \sum_{i}^{N_s} z_i Y_i \tag{15}$$

where N_s is the total number of species, and $\mathcal{C}_i$ and z_i are constant coefficients for every species. For each species i, Le_i is assumed to be non-unity, but constant along the flamelet. The molecular diffusion fluxes of the controlling variables are therefore expressed as:

$$\mathbf{j}_c = -\frac{\lambda}{c_p}\nabla\left(\sum_{i=1}^{N_s-1}\frac{\mathcal{C}_i - \mathcal{C}_{N_s}}{\mathrm{Le}_i}Y_i\right) = -\frac{\lambda}{c_p}\nabla\beta_c,$$
$$\mathbf{j}_z = -\frac{\lambda}{c_p}\nabla\left(\sum_{i=1}^{N_s-1}\frac{z_i - z_{N_s}}{\mathrm{Le}_i}Y_i\right) = -\frac{\lambda}{c_p}\nabla\beta_z, \tag{16}$$

where $\mathcal{C}_{N_s}$ is the coefficient of the most abundant species, N_2 for the present study. The above equations take thus the form of diffusive transport terms depending on the gradient of the β_c and β_z parameters. The diffusive behaviour of all species in the LES can now be taken into account by tabulating the additional parameters β_c, β_z and the λ/C_p ratio. In the definition employed here, the progress variable only depends on water and it is scaled, so that $\mathcal{C}_{\mathrm{H_2O}} = 1/\psi_{\max}(z)$ and $\mathcal{C}_i = 0$ for every other species. For the jet-in-coflow partially premixed case, water is also present in the reactants. Thereofore, considering the definition in Equation (2), the expression for β_c becomes:

$$\beta_c = \frac{Y_{\mathrm{H_2O}} - Y^{\mathrm{reac}}_{\mathrm{H_2O}}}{\mathrm{Le}_{\mathrm{H_2O}}\,\psi_{\max}(z)} \tag{17}$$

A similar procedure is followed for the enthalpy equation, where the heat flux $\mathbf{q}$ can be written as:

$$\mathbf{q} = -\lambda\nabla T - \left(\sum_{i=1}^{N_s-1}(h_i - h_{N_s})\frac{1}{\mathrm{Le}_i}\frac{\lambda}{C_p}\nabla Y_i\right) \tag{18}$$

where h_i is the enthalpy of species i. In the above equation, the first term on the right-hand side is the conductive flux, while the second term describes the redistribution of enthalpy associated with the different diffusion of species. Following the derivation in [30] the above equation can be rewritten as :

$$\mathbf{q} = -\frac{\lambda}{C_p}\left(C_p - \sum_{i=1}^{N_s-1}\frac{c_{p_i} - c_{p_{N_s}}}{\mathrm{Le}_i}Y_i\right)\nabla T - \frac{\lambda}{C_p}\nabla\left(\sum_{i=1}^{N_s-1}\frac{h_i - h_{N_s}}{\mathrm{Le}_i}Y_i\right)$$
$$= -\frac{\lambda}{C_p}\beta_{h_1}\nabla T - \frac{\lambda}{C_p}\nabla\beta_{h_2}, \tag{19}$$

where c_{p_i} refers to the specific heat capacity at a constant pressure of species i. The two terms on the right-hand side in the above equation represent differential diffusion effects

on the heat flux due respectively to local redistribution of specific heat and enthalpy, and to the diffusion of species within the mixture. The final set of modified equations for control variables and enthalpy solved in the LES is:

$$\begin{aligned}
\overline{\rho}\frac{D\widetilde{c}}{Dt} &= \nabla\cdot\frac{\mu_t}{Sc_t}\nabla\widetilde{c} + \nabla\cdot\bar{\rho}\widetilde{\mathcal{D}}\nabla\widetilde{\beta}_c + \overline{\dot{\omega}_c} \\
\overline{\rho}\frac{D\widetilde{z}}{Dt} &= \nabla\cdot\frac{\mu_t}{Sc_t}\nabla\widetilde{z} + \nabla\cdot\bar{\rho}\widetilde{\mathcal{D}}\nabla\widetilde{\beta}_z \\
\overline{\rho}\frac{D\widetilde{h}}{Dt} &= \nabla\cdot\left(\frac{\mu_t}{Pr_t}\right)\nabla\widetilde{h} + \nabla\cdot\left(\bar{\rho}\widetilde{\mathcal{D}}\widetilde{\beta}_{h_1}\nabla\widetilde{T} + \bar{\rho}\widetilde{\mathcal{D}}\nabla\widetilde{\beta}_{h_2}\right)
\end{aligned} \tag{20}$$

The filtered coefficients $\widetilde{\beta}_i$ and the filtered diffusivity $\widetilde{\mathcal{D}}$ in the equations above are obtained from the flamelets computations, pre-integrated according to Equation (5) and tabulated. Further details on the flamelets database are given in the next section.

3.3. *Flamelets database*

The thermochemical databases for the two study cases described in Section 2 are built using 300 premixed freely propagating laminar 1D flamelets with reactants equivalence ratios spanning the flammability range. For both the study cases temperature and species mass fractions in the reactants vary linearly with the mixture fraction, between their value in the oxydiser stream, where $z = 0$, to the value in the fuel stream, for which $z = 1$, as reported in Tables 1 and 2. Therefore, for the premixed slot burner case, all the flamelets have a constant reactant temperature of 300 K and the composition varies linearly between pure air and pure hydrogen, over a flammability range of $z = [0.007,\ 0.17]$. The stoichiometric condition is found at $z_{\text{st}} = 0.028$. For the partially premixed lifted flame case, the flamelets' reactants temperature varies between 305 K in the fuel stream and 1045 K in the oxydiser stream (hot coflow). The reactants on the leaner flamelets are therefore at higher temperatures and with a higher content of water, which is present in the coflow. In this case the mixture fraction spans a flammability range in $z = [0.1,\ 0.75]$, with stoichiometric conditions at $z_{\text{st}} = 0.474$. It is worth noting that the high diffusivity of hydrogen can affect the mixing between fuel and oxydiser ahead of the flame, so that the reactants' mixture composition and enthalpy may not vary linearly with mixture fraction. However, the inert jet/coflow mixing was shown in [36, 43] to be about linear with mixture fraction, due to the high content of nitrogen in both streams. The high temperature and water content at low mixture fraction values create a peculiar reaction rate map with a peak on the lean side, as shown in Figures 5 and 6b. Also, the effect of species non-unity Lewis number assumption on this database differs from the hydrogen/air case at constant temperature, shown earlier in Figures 3–4. It can be seen from Figure 6(a) that the mixture fraction decrease along each flamelet is lower than in the hydrogen/air case shown in Figure 4, due to the relatively lower hydrogen content in the reactants associated with the presence of water, and higher content of nitrogen in the reactants. Moreover, Figures 5 and 6b show that the inclusion of differential diffusion in the database results in a decrease in the reaction rate and its peak value for the lean flamelets, and a slight increase on the rich side. Also, when non-unity species Lewis number is considered in the manifold, the progress variable range over which the reaction occurs results to be slightly narrowed on the lean side as compared to the unitary Lewis number case, while it appears broadened for rich mixtures. In a partially premixed case like the lifted flame in hot coflow, the flame stabilisation is controlled

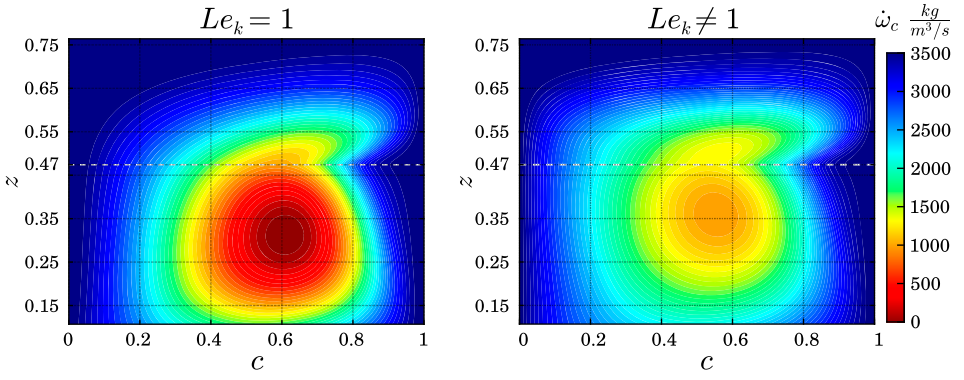

Figure 5. Contour plots of the scaled progress variable reaction rate in the $c-z$ space for the flamelet database of the jet/coflow case with reactants conditions reported in Table 2. Flamelet calculations with unity Lewis number (left) and mixture averaged diffusion model (right). Results obtained using San Diego meachanism [60]. The stoichiometric condition, $z_{\text{st}} = 0.474$, is marked with the white dashed line.

by the equilibrium between convection and reaction rate associated with the local mixture fraction and progress variable values. Variations in these characteristic maps are therefore expected to affect the location at which the flame stabilises.

A parametric analysis in [40] further revealed the importance of the chosen kinetic mechanism on the lifted flame predictions. In the present work, the kinetic mechanisms DRM19 [61], Li et al. [62], Ó Conaire [63], and San Diego [60] were tested *a-priori* in the flamelet calculation and a sensitivity of the reaction rate map in terms of peak value and distribution in the progress variable/mixture fraction space was observed, in particular under the non-unity Lewis number assumption. Therefore, the effects of the inclusion of differential diffusion in the database can depend on the chosen kinetic mechanism. San Diego mechanism was selected for all the simulations of the partially premixed case, following the aforementioned analysis and previous studies on hydrogen flames. Interested readers can find the comparisons of different mechanisms in Appendix 2. For the premixed slotted burner the mechanism by Burke et al. [56] is used instead, in order to remain consistent with the reference DNS in [25].

4. Numerical details

The Favre-filtered Navier Stokes equations including conservation of mass, momentum and absolute specific enthalpy (sum of sensible and formation enthalpies) are solved together with the transport equations of the controlling variables described in Section 3 using the low-Mach approximation and the finite volume method implemented in OpenFOAM v9. The filtered temperature is computed from the absolute enthalpy using the theorem of the integral mean as done in previous works (e.g. see [35]): $\widetilde{T} = T_0 + (\widetilde{h} - \Delta\widetilde{h}_f^0)/\widetilde{C_p^{eff}}$, where $T_0 = 298.15\,\text{K}$ is the reference temperature. The mixture enthalpy of formation Δh_f^0 and the mixture effective specific heat at constant pressure $C_p^{eff} = \int_{T_0}^{T} C_p(T')dT'/(T - T_0)$ are computed from the 1D laminar flamelets. The filtered values of these quantities are obtained through pre-integration consistently with Equation (5) and tabulated. The mixture density is then calculated enforcing the ideal gas equation of state

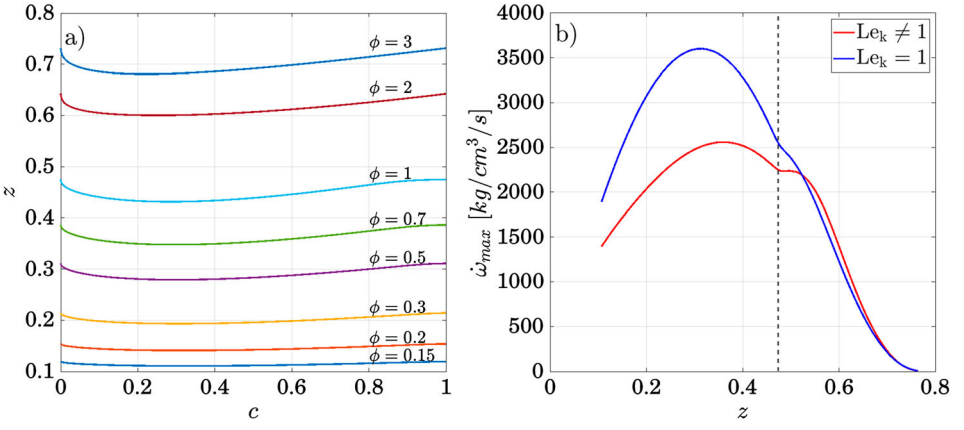

Figure 6. (a) Variation of mixture fraction in progress variable space across a freely propagating flame at different equivalence ratios, with the boundary conditions dfined in Table 2. (b) Maximum reaction rate at different reactants mixture fraction values obtained with and without differential diffusion modelling. Results obtained using the San Diego kinetic mechanism [60]. The stoichiometric condition $z_{st} = 0.474$ is marked as a vertical black dashed line.

$\bar{\rho} = p_o \widetilde{W}/R_0 \widetilde{T}$, where the filtered mixture molecular weight $\widetilde{W}$ is also computed from the 1D flamelets, pre-integrated and tabulated, and p_o is the operative pressure.

The pressure implicit with the splitting operator (PISO) [64] algorithm is used for the pressure/velocity coupling and an external loop with at least 5 iterations per time step is used for the solution of the scalar transport equations. Second-order central schemes are used for all convective terms, with a Gamma limiter applied to the regions of high gradients across the flame. An implicit Euler scheme is used for temporal discretisation, following previous works [34, 35]. A constant time step is used to ensure a maximum CFL number below 0.35 everywhere in the computational domain. This corresponds to a timestep in the LES of $\Delta t = 2.0 \times 10^{-7}$ s for the lifted flame and $\Delta t = 1.0 \times 10^{-6}$ s for the slot burner. The subgrid-scale stresses in the filtered momentum equation are closed using a one-equation model as in [35]. The one-dimensional solver CHEM1D [65] is used for the flamelets computation, with the kinetic mechanisms described in Section 3. For the construction of the 4D table, $n_c = 100$ equispaced discretization points between 0 and 1 are used in the progress variable space, and $n_{\sigma_c} = 50$ points spanning between 0 and $\widetilde{c}(1-\widetilde{c})$ are used for its subgrid variance space. The filtered mixture fraction space spans the flammability range, and a total of $n_z = 160$ and $n_z = 100$ equispaced discretization points are used for the lifted flame and the slot burner case, respectively. A total of $n_{\sigma_z} = 15$ points are used for the mixture fraction subgrid variance, spanning exponentially the range $[0, \widetilde{z}(1-\widetilde{z})]$. Outside the flammability limits a linear interpolation of the tabulated quantities to their value in the fuel and oxydizer streams is performed.

The numerical domain for the lifted flame, shown in Figure 2(b), is a cylinder with a diameter of 183 mm (corresponding to 40 nozzle diameters D), which extends axially from the nozzle outlet to $50D$ downstream. The hot coflow enters the domain through an annular section extending radially from $0.5D$ to $20D$. The mesh distribution is chosen following previous LES works [40, 43] and consists of $N_x \times N_r \times N_\theta = 230 \times 60 \times 80$ cells in the axial, radial and azimuthal directions respectively, amounting to 897 ,000 cells in total. The cells are non-uniformly distributed so to cluster in the region of interest (up to

$30D$ in the axial direction), and the spacing in the streamwise and radial directions, $\Delta_x \approx 0.6$ mm, $\Delta_r \approx 0.4$ mm, respectively, is of the order of the laminar flame thickness $\delta_l \approx 0.66$-1 mm. Pope's 80% turbulent kinetic energy criterion [66] was applied on preliminary simulations to assess the quality of the mesh. The ratio between modelled, k_{SGS}, and total turbulent kinetic energy (resolved plus SGS) was found below 0.2 in the region of interest. Boundary conditions for the lifted flame case are shown in Figure 2(b). A turbulent inlet velocity profile is imposed at the nozzle exit, with synthetic turbulence imposed using the approach in [67]. The synthetic eddies generator takes a target of mean velocity profile, rms velocity profile and an integral length scale as input. The measured average turbulent axisymmetric velocity profile reported in [38–40] is imposed at the nozzle outlet. The measured profile is scaled to ensure that the massflow rate at the inlet of the domain equals that in the experimental case. The flame lift-off height was observed to be very sensitive to the turbulent inlet condition [40]. For this reason a preliminary analysis is carried out to ensure an accurate prediction of the jet spreading rate and its mixing with the coflow, and details of this analysis can be found in Appendix 1. As result of this analysis, other than the axial and radial rms velocity profiles, u' and v', measured in [39], an integral length scale of $l_0 = 0.07D$ is imposed as a target of the synthetic turbulence generator. Atmospheric pressure is imposed at the outlet, while zero-gradient conditions are imposed on outlet and lateral boundaries for all other scalars. Temperatures of 305 and 1045 K are assigned at the jet and coflow inlets respectively, according to the experiment. The progress variable is set to zero at the inlets, and ignition is artificially imposed by creating a cylindrical sub-region in the domain with $\widetilde{c} = 1$. The mixture fraction is 1 at the jet inlet and 0 in the hot coflow. Each LES is run for a period of 4 flow-though times, defined as the time needed by a parcel of fluid travelling at the bulk speed on the centreline to reach a location of $40D$ downstream, approximately $t_{flow} \approx 16$ ms. Of these, one is used to pass the transient after ignition and the remaining three to collect statistics. Time-averaged data is further averaged azimuthally exploiting the axial symmetry of the domain.

The computational domain for the premixed slot burner case is shown in Figure 2(c). The reactants nozzle has a height of $H = 8$ mm and a width of $4.5H$ in the z direction, and the rim has a thickness of 0.4 mm. A portion of the channel flow upstream of the nozzle exit, of length $2H$, is included in the domain. The domain is $12.5H$ long in the y direction and it extends for $15H$ downstream in the x direction. A structured hexaedral mesh is used with $N_x \times N_y \times N_z = 274 \times 140 \times 123$ cells in the three directions, respectively, amounting to a total of 4.8M cells. The cells are non-uniformely distributed to guarantee a size ranging from 0.2 to 0.5 mm in the flame region, where the estimated laminar flame thickness is $\delta_l \approx 0.66$ mm. In the y direction, 32 cells are placed across the channel width. The imposed boundary conditions are also shown in Figure 2(c). Atmospheric pressure with zero gradient velocity is imposed at the outlet, while symmetry conditions are imposed on all the lateral surfaces. The mixture fraction is imposed to $z = 0.0116$ ($\phi = 0.4$) at the inlets. The temperature is set to 300 K at the reactants inlet and to 1425 K at the products stream inlet. A uniform velocity of 3.6 m/s is imposed at the products stream inlet. A constant temperature of 300 K is imposed at the nozzle walls, together with no-slip conditions for the velocity field. The same strategy as for the lifted flame case is used to impose synthetic turbulence at the nozzle inlet. In this case, a preliminary LES of a developed turbulent channel flow, with velocity of $U_{bulk} = 24$ m/s, is performed to obtain average and rms velocity profiles to impose to the synthetic turbulent inflow generator. Only instantaneous fields are analysed in this case, therefore the LES are run for just two flow-through times of $t_{flow} = 5$ ms.

5. Results

5.1. *Slot burner*

The lean fully premixed slotted burner studied in [25] is simulated under the conditions reported in Table 1 employing two of the differential diffusion modelling approaches introduced in Section 3.2 and summarised in Table 3. Differential diffusion effects were clearly observable in the DNS of this case [25], when compared to the equidiffusive case, for the occurrance of superadiabatic temperatures and self-wrinkling due to thermodiffusive instabilities, ultimately leading to a shorter flame length. The objective here is to investigate if the two modelling strategies are able to mimic these effects, in particular the coupling of curvature and mixture fraction redistribution at the resolved level, for a typical filter size of the order of the laminar flame thickness, at least from a qualitative point of view. In both models, the effects of differential diffusion are included at the thermochemistry level by assuming non unity Lewis number for every species, $\mathrm{Le}_k \neq 1$, in the flamelet computation, using Equation (11). In the first model, $\mathrm{M1_{RES}}$, a source term $\overline{\dot{\omega}}_z$ is added to the mixture fraction transport equation, together with a modified diffusion coefficient D_z in line with the work in [5]. The mixture fraction source term is computed by directly using the resolved LES quantities in Equation (13). In the second approach, M2, the model proposed by Van Oijen and coworkers [30] is employed and extended to the LES context. A correction on the molecular diffusion flux is applied in this case to the transport equations of the controlling variables and enthalpy, as introduced in Section 3.2.

A qualitative comparison of instantaneous temperature and mixture fraction fields obtained using the two models is shown in Figures 7 and 8, respectively, at random times. Both models appear to be able to reproduce the occurrence of super-adiabatic temperatures downstream of the flame front. These are predicted to be around 1600–1700 K by

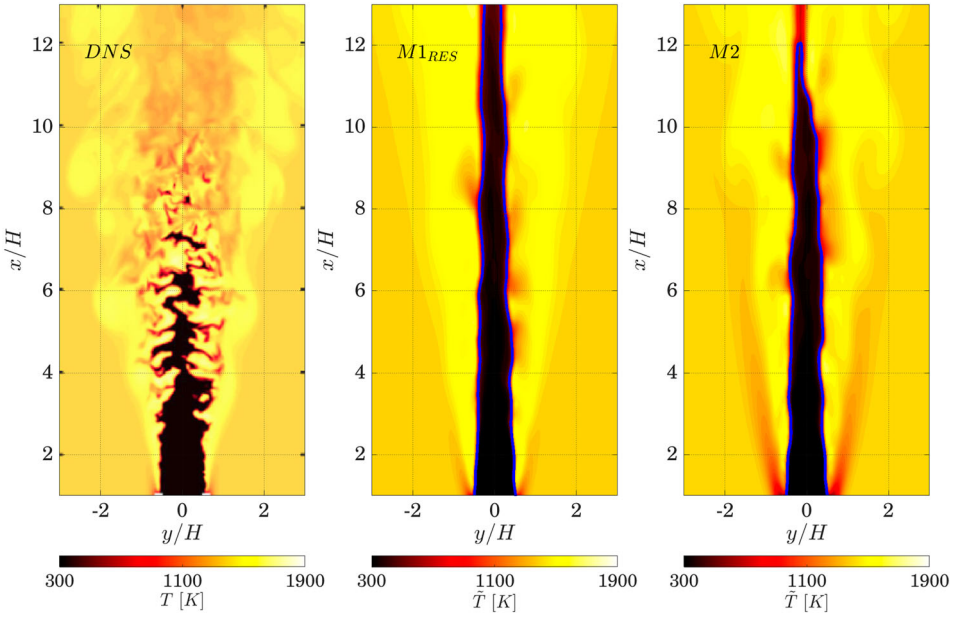

Figure 7. Midplane temperature contours from DNS [25] (left), and LES cases $\mathrm{M1_{RES}}$ (centre) and M2 (right) of Table 3. Line: progress variable isoline $\tilde{c} = 0.5$ (−).

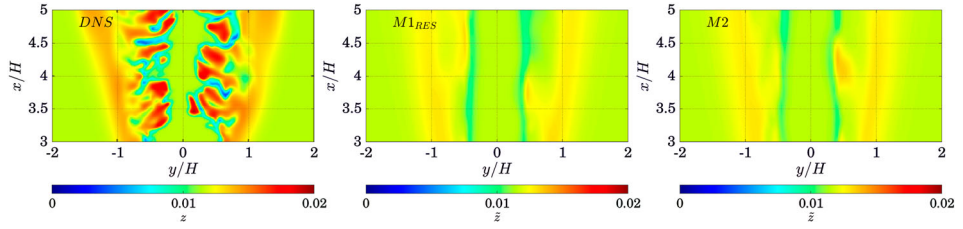

Figure 8. Midplane mixture fraction contours form DNS [25] (left), LES model $M1_{RES}$ (centre) and LES model M2 (right) of Table 3.

Table 3. Differential diffusion models used for the LES of the slot burner case [25].

	$M1_{RES}$	M2
Flamelets	$Le_k \neq 1$	$Le_k \neq 1$
LES	correction of $\tilde{z}$ only	correction of $\tilde{c}$, $\tilde{z}$ and $\tilde{h}$
	Equations (12)–(14)	Equations (16)–(19)

both models, in reasonable agreement with DNS results, reporting peak temperature values around 1700 K. The presence of temperatures higher than equilibrium (1425 K) can be only obtained by allowing local changes in the mixture fraction and using a chemistry database spanning a broader range of reactants mixture fraction values with $Le_k \neq 1$. Both models appear to be able to capture the coupling effect between flame front curvature and differential diffusion, giving rise to the development of thermo-diffusive instabilities in the form of bulges. From the contour plots in Figure 8 it can be seen how the mixture fraction locally deviates from the nominal value of $z = 0.0116$ ($\phi = 0.4$) with a decrease upstream of the flame front and a re-increase towards the products. This also occurs in flat regions of the flame surface and is in line with what can be observed in 1D laminar flamelets in Figure 4 and in [5]. In agreement with DNS results and previous studies [7, 9], in the two LES cases a positive (convex) curvature towards the reactants is associated with a mixture enrichment and increase in temperature, while cusps are related to leaner mixture and to temperature and reaction rate reduction. Despite their different formulations, both models lead to very similar predictions in terms of flame front local curvature, broadening of mixture fraction range around the nominal value and super adiabatic temperature peaks, although model M2 predicts a mildly shorter flame. This can be assessed by looking at Figure 7, where the flame front identified by the progress variable isoline $\tilde{c} = 0.5$ shows a tip at around $13H$ for model M2, while it appears still open throughout the whole computational domain for model $M1_{RES}$. These results suggest that accounting for modification only in the mixture fraction field (model $M1_{RES}$) is sufficient to predict the correct coupling with curvature, at least for fully premixed cases without other sources of enthalpy variations. Additional considerations will be provided for the partially premixed cases of Section 5.2.

Overall, the flame predicted by the two LES models appears less wrinkled than in the DNS, which is directly connected to an underestimation of flame surface area and global consumption rate, ultimately leading to a longer flame. Note that the DNS data was not prefiltered in Figure 7, which partly explains why the formation of bulges in the LES occurs at larger scales with respect to the DNS. Results further suggest that, although the coupling

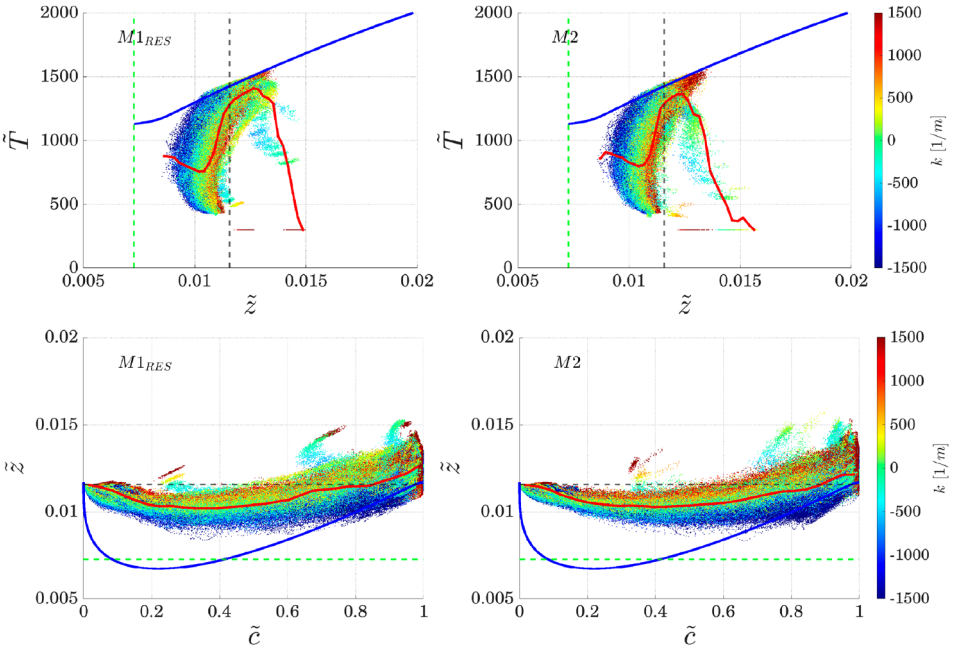

Figure 9. Scatter plots of filtered temperature versus filtered mixture fraction (top) and mixture fraction versus filtered progress variable (bottom) obtained from the LES of the premixed slot burner using the two differential diffusion approaches of Table 3. Only values within the flame, identified using $0.1<\widetilde{c}<0.9$, are considered. The black and green dashed lines mark the nominal mixture fraction, $z = 0.0116$, and the lean flammability limit, $z_l = 0.007$, respectively. In the upper plots, the blue line represents the equilibrium temperature at different reactant mixture fraction values. In the bottom plots, the blue line represents the mixture fraction values along the progress variable computed for an unstretched laminar premixed 1D freely propagating flamelet at nominal reactants equivalence ratio $\phi = 0.4$, with the mixture-averaged model to account for differential diffusion, see Figure 4. The red line represents the conditional average.

leading to flame surface growth is captured qualitatively, additional wrinkling is necessary for LES filter resolution of the order of the flame thickness. This implies that to obtain the correct flame surface area additional modelling for the coupling between differential diffusion and flame curvature at the subgrid level (e.g. see [11]) is needed. This is beyond the scope of the present work where the interest is limited to the prediction of mixture fraction and enthalpy redistribution, and may be explored in future studies.

To further compare the influence of the two differential diffusion approaches of Table 3 on the predicted reacting states in the LES, scatter plots of filtered temperature and progress variable versus mixture fraction are reported in Figure 9, together with their conditional averages. Temperature values are reported only in the region of the flame, identified for simplicity here by $0.1<\widetilde{c}<0.9$. The scatter plots are coloured by the local flame front curvature in order to investigate the coupling between self-wrinkling and diffusive transport. The filtered (resolved) curvature k is defined as [25] $k = \nabla \cdot \mathbf{n}$, where $\mathbf{n} = -\nabla\widetilde{c}/|\nabla\widetilde{c}|$ is the unit vector normal to the flame front and pointing towards the reactants.

Scatter plots of the progress variable versus mixture fraction are further reported in Figure 9 (bottom), showing that both models appear capable of describing the mixture fraction decrease ahead of the flame front across the progress variable space and its return to

the nominal value in the products, $\widetilde{z} = 0.0116$ (black dashed line in the figure). This effect of differential diffusion is also observable for an unstretched premixed flamelet (blue line in the figure) and is observed from the LES in the zero curvature burning states along the progress variable values in the same figure. Moreover, both models describe the interplay between flame front curvature and differential diffusion, which can be appreciated by the broadening of the mixture fraction values range around the values corresponding to zero curvature states. A positively curved flame front towards the reactants leads to richer burning states, while negative curvature values (cusps) are associated with a decrease in mixture fraction, in line with DNS results. In particular, the LES is able to capture two features observed in the DNS [25] at high values of the progress variable $\widetilde{c}>0.8$, and associated with curvature effects:

- Burning states richer than the nominal mixture fraction, with an overshoot in the mixture fraction conditional average with respect to the nominal value, achieved through positive flame front curvature (red dots),
- Burning states at mixture fraction values leaner than the laminar unstretched flamelet (blue line), as an effect of the negatively curved flame front sections (cusps, blue dots).

The same effects are also observed in the temperature scatter plots. The prediction of superadiabatic temperature is associated with the richer mixture reaching the equilibrium temperature. As qualitatively observed in Figure 8, these rich burning states are caused by the coupling of mixture fraction diffusive flux and positive flame front curvature towards the reactants. In correspondence with flame cusps (regions of negative curvature towards the reactants) conditional temperature and reaction rate decrease instead.

Despite their different formulations, the two models give very similar predictions, with almost overlapping conditional averages. In particular, model M2 predicts states at slightly higher progress variable and temperature for mixture fraction values leaner than the nominal value, as compared to model $\mathrm{M1}_{\mathrm{RES}}$. These are associated with negative flame front curvature and suggest a more frequent occurrence of cusps predicted by model M2, which in turn can be explained by the correction in progress variable diffusion flux in model M2.

The analysis above shows that both models of Table 3 are able to mimic qualitatively the differential diffusion effects on local redistribution of mixture fraction and, up to a certain extent, thermodiffusive instability, at the resolved level in a well-resolved LES of turbulent premixed flame. For such a case the corrections on the molecular diffusion in the controlling variables transport equations appear to be non-negligible with respect to the turbulent transport. As already observed from the contour plots in Figures 7 and 8, the differential diffusion effects predicted by the two LES models appear to be milder than what was observed from DNS results [25]. In general, the mixture fraction range around the nominal value is quite narrow and at low progress variable values the zero curvature burning states do not reach the lean mixture fraction values corresponding to the laminar unstretched flamelet. This suggests that the corrected diffusive flux of the controlling variables imposed by the two models may be too mild, being it only dependent on the resolved curvature. As mentioned earlier, a model for the interaction between curvature and differential diffusion at the subgrid level may provide higher resolved diffusive fluxes, ultimately leading to better LES predictions in terms of mixture fraction redistribution and flame front wrinkling. The effects of an increase of the diffusive fluxes corrections in model M2, for example associated with the use of a subgrid differential diffusion model, are shown in a sensitivity analysis reported in Appendix 3. In the next section, modelling approaches

Table 4. Differential diffusion (DD) models used for LES and flamelets.

	MLe1	M0	$M1_{RES}$	$M1_{TAB}$	M2
Flamelets	$Le_k = 1$	$Le_k \neq 1$	$Le_k \neq 1$	$Le_k \neq 1$	$Le_k \neq 1$
LES	no DD	no DD	$\widetilde{z}$ corrected Equation (13) resolved	$\widetilde{z}$ corrected Equation (13) tabulated	$\tilde{c}, \tilde{z}, \tilde{h}$ corrected Equations (16)–(19)

for differential diffusion are tested on a partially premixed lifted flame at higher turbulence conditions, where variations of mixture fraction are also due to the turbulent mixing between jet and coflow and it is unclear whether this would hinder or strengthen the effects of differential diffusion.

5.2. *Lifted flame in vitiated coflow*

5.2.1. *Flame structure*

The lifted flame in vitiated coflow [36] under the conditions reported in Table 2 is first simulated with the assumption of $Le_k = 1$ for all species k both in the thermochemical database and in the LES equations (*MLe*1 model in Table 4). In this case, the LES predicts a lifted flame stabilising at about $x = 10D$, as can be seen from both instantaneous and time-averaged temperature contours in Figure 10. In this setup, the fuel jet mixes with the oxidiser in the coflow until the mixture enters the flammability range and the flame stabilises in regions where the reaction rate and local convective transport balance each others. Flame stabilisation location and flame length can be further assessed by looking at the average reaction rate contour plots, also shown in Figure 10. A region of strong mean reaction rate, $\langle\widetilde{\omega}_c\rangle = 980\,\mathrm{kg/m^3/s}$ is observed at the flame base, in correspondence of lean premixed conditions, $\langle\widetilde{z}\rangle = 0.25$. The inner part of the flame brush is observed instead to burn close to stoichiometric conditions or slightly rich, but with milder values of reaction rate. This stabilisation mode is consistent with other studies in literature [68], identifying a triple point at the base of the flame and an inner branch stabilising in diffusion mode.

Turbulent mixing and reaction processes can be further assessed by comparing average and rms mixture fraction values along the centreline obtained from the LES with those from experimental measurements [40]. These comparisons are shown in Figure 11. The central jet can be divided in a region of inhert jet/coflow mixing, followed by a reactive zone and a downstream region where the products of combustion mix with the coflow stream. As the fuel jet spreads and mixes with the coflow, the predicted centreline mixture fraction decreases at the correct rate from $\tilde{z} = 1$ at the fuel nozzle exit to around $\tilde{z} = 0.8$ at flame anchoring point ($x = 10D$). At this location the flow accelerates due to thermal expansion and a decrease in the rate of jet spreading and centreline mixture fraction decay is correctly captured by the LES. Similarly, the mixture fraction rms along the centreline increases from the nozzle outlet due to turbulent mixing and reaches a local maximum in correspondence with the flame base, which is also well predicted by the LES. The average temperature values on the centreline in Figure 11 as predicted by the LES are also in very good agreement with the experimental results. The rate of temperature increase in the streamwise direction due to inert jet/coflow mixing is well captured until the flame base location at $x = 10D$. The temperature then reaches a maximum value of 1500 K at the

flame tip, followed by a slight decrease due to the mixing between the combustion products and the coflow stream. The temperature rms peak and its location are also predicted well by the LES. This quantity increases first due to turbulent inert mixing followed by a steeper gradient near the flame base, and then decreases downstream, where the mixture temperature becomes more homogeneous.

Computed radial profiles of average and rms temperature and mixture fraction are compared to experimental values in Figure 12. A very good agreement between LES and experiments is observed for the average mixture fraction and its rms at any axial location, suggesting that the LES correctly captures the shear layer thickness and its development between jet and coflow. For the temperature profiles, a good agreement between LES results and experiments is found at $x = 8D$, where inert jet/coflow mixing takes place and a peak of rms temperatureT_{rms} is observed on the shear layer. In the experiment, the flame base is observed around $x = 11D$. The presence of the flame can be identified in these plots by the overshoot of temperature with respect to its value in the coflow stream. As can be observed from the figure at $x = 11D$, the LES slightly overepredicts the flame lift-off height, which also results in a more significant underestimation of temperature rms at $x = 11D$. For more downstream locations, however, both temperature and its rms are well reproduced by the LES, including the double peak in the $\widetilde{T}_{rms}$ profile observed at $x = 14D$, identifying the inner flame branch and outer mixing layer between combustion products and hot coflow.

The above comparisons suggest that the premixed flamelets with presumed FDF approach without differential diffusion treatment are already satisfactory to predict the main flame features for this test case. With respect to the slot burner analysed in Section 5.1, the lifted flame analysed in this section is characterised by higher levels of turbulence and it is highly controlled by turbulent mixing, which might hinder the effects of differential diffusion observed in Section 5.1. The influence of differential diffusion modelling on the predicted flow field is thus investigated next to shed light on this point.

5.2.2. *Differential diffusion modelling*

Further simulations of the lifted flame were performed to assess the relevance of differential diffusion models on the prediction of flame features. In addition to model MLe1 introduced earlier, four modelling approaches are tested and summarised in Table 4. Models M1_{RES} and M2 are the same used in Section 5.1 and listed in Table 3. In model M0 the flamelets database is built by considering non-unity Lewis number for every species, $\text{Le}_k \neq 1$, but no differential diffusion model is included in the LES transport equations. This way the influence of the themrochemistry on the results can be assessed, as it was shown in Figure 5 that the reaction rate of progress variable varies significantly between the cases with $\text{Le}_k \neq 1$ and $\text{Le}_k = 1$. Model M1_{TAB} uses the model in [5] to quantify the variation of mixture fraction distribution, as for model M1_{RES}, where however term $\overline{\dot{\omega}_\zeta}$ in Equation (13) is computed from flamelets, pre-integrated and tabulated consistently with Equation (5).

Mean centreline and radial profiles of temperature, mixture fraction and their rms as predicted by the five models of Table 4 are compared to experimental data in Figures 11 and 12 respectively. The mixture fraction decay along the centreline, associated mainly with mixing between jet and coflow streams, is captured fairly well by all models. Interestingly, the models including differential diffusion at the resolved level M1_{RES}, M1_{TAB} and M2, predict a slightly steeper mixture fraction axial decay rate and temperature increase in the

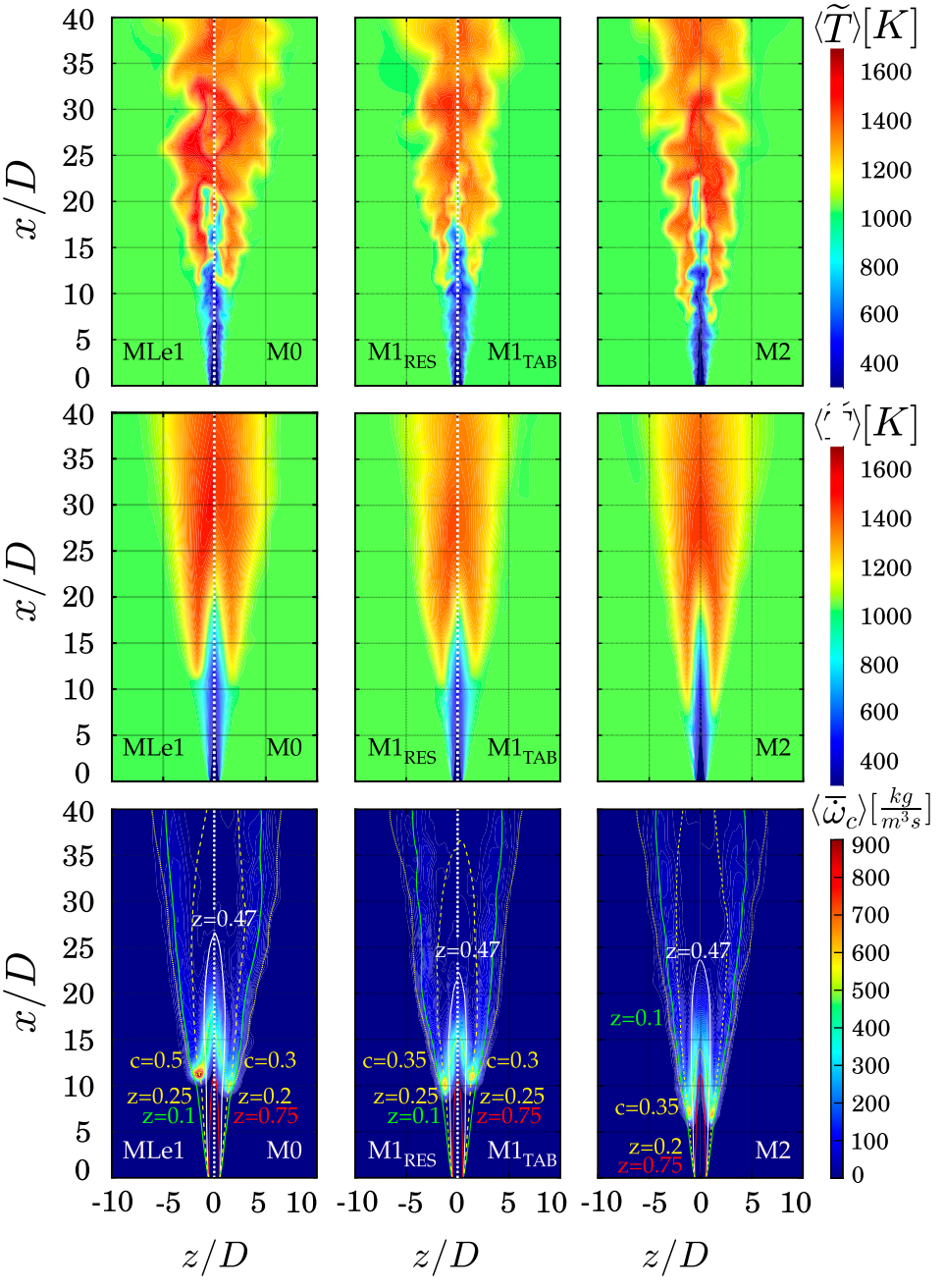

Figure 10. Mid-plane contours of instantaneous (top), time-averaged (centre) temperature, and averaged filtered reaction rate (bottom) obtained from LES using the models for differential diffusion of Table 4. Solid isolines represent lean flammability limit (–, $\langle\tilde{z}\rangle = 0.1$), rich flammability limit (–, $\langle\tilde{z}\rangle = 0.75$), and stoichiometric condition (white line, $\langle\tilde{z}\rangle = 0.47$). Dashed isolines represent the progress variable $\langle\tilde{c}\rangle$ (· · ·) and mixture fraction $\langle\tilde{z}\rangle$ (– –) at the location of maximum reaction rate.

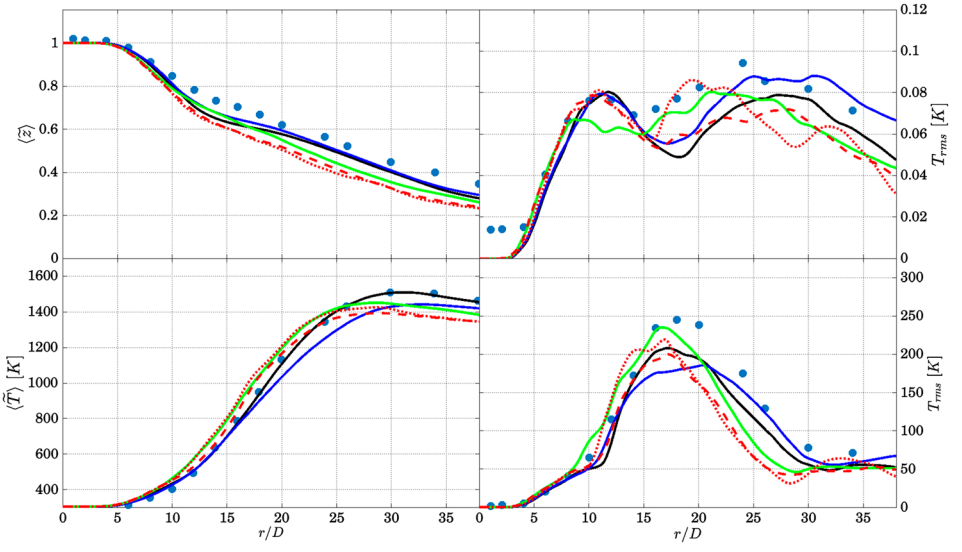

Figure 11. Centreline profiles of mean and rms temperature and mixture fraction. Symbols: measurements [36]. Lines: LES results from models MLe1 (−), M0 (−), M1$_{\mathrm{RES}}$ (···), M1$_{\mathrm{TAB}}$ (− −), and M2 (−) of Table 4.

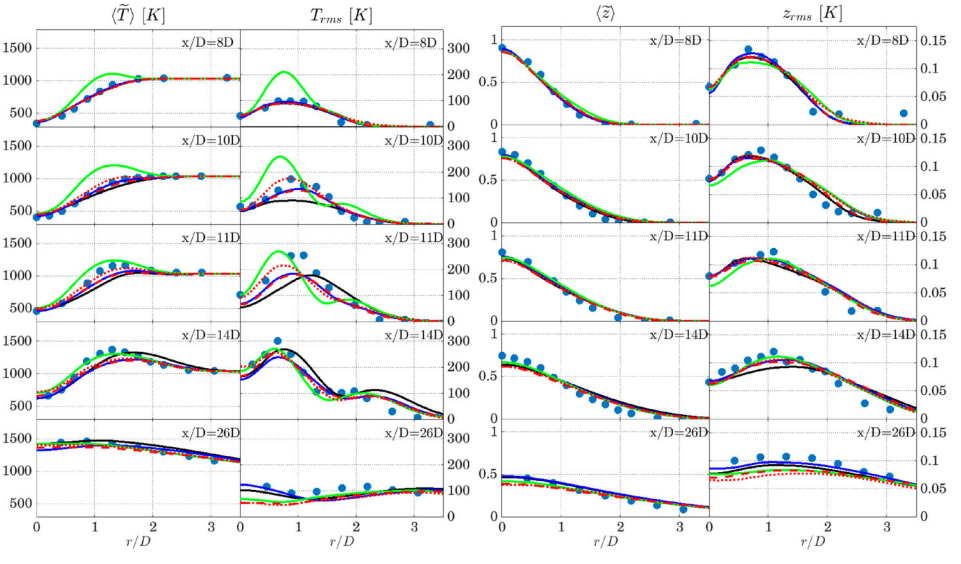

Figure 12. Radial profiles of time-averaged and rms values of temperature and mixture fraction. Symbols: measurements [36]. Lines: LES results with model (−) *MLe*1, (−) *M*0, (···) *M* 1$_{\mathrm{RES}}$, (− −) *M* 1$_{\mathrm{TAB}}$, (−) M2.

region upstream of the flame base, $4D<x<10D$, as compared to models MLe1 and M0. This reveals that the predicted inert jet/coflow mixing is mildly enhanced by the modified diffusive terms in the controlling variable transport equations. For similar reasons a slightly steeper increase of mixture fraction rms is observed for models M1$_{\mathrm{RES}}$, M1$_{\mathrm{TAB}}$ and M2. These differences in the inert mixing cause the flame to stabilise slightly more upstream

in the cases with enhanced diffusive flux, which in turn results in the differences observed between the various models downstream of the flame stabilisation point ($x>10D$). The direct comparison between models M0 to MLe1 of Table 4 further highlights the effect including differential diffusion in the thermochemistry. As observed in Figure 11, model M0 predicts the flame stabilisation point slightly more upstream, at $x \approx 10D$ as compard to $x \approx 11D$ predicted by model MLe1. Moreover, the flame for case M0 is slightly longer, see temperature contours in Figure 10. Also, mean temperature along the centreline increases at a slower rate for model M0 as compared to MLe1, and reaches a lower peak value. Similar considerations can be made by looking at radial profiles in Figure 12. This different behaviour is explained by an overall reduction of reaction rate values when non-unity Lewis number is used in the flamelet database, as observed in Figure 5. Nevertheless, model M0 also predicts the flame stabilisation point more upstream than model MLe1 as discussed earlier, which would suggest a higher reaction rate instead. This is explained as follows. From Figure 5, when differential diffusion is taken into account ($\mathrm{Le}_k \neq 1$), the peak value of reaction rate decreases by about 30% as compared to the case at $\mathrm{Le}_k = 1$, but its location also shifts towards the stoichiometric condition and lower values of the progress variable, $c \approx 0.55$, in the $c-z$ space. For $c<0.4$ the reaction rate in the case with differential diffusion is weaker on the lean side ($z<0.25$) and stronger on the rich side ($z>0.47$). By looking now at the reaction rate contours in Figure 10, one can notice that the intensity of the reaction rate at the flame base on the lean premixed side decreases by around 47% for model M0 as compared to model MLe1, while it is about the same in the innermost rich region. The highest reaction rate at the flame base is found for $\langle\widetilde{c}\rangle \approx 0.3$ in model M0 as compared to $\langle\widetilde{c}\rangle \approx 0.5$ for model MLe1, and at slightly leaner conditions ($\langle\widetilde{z}\rangle \approx 0.20$ as compared to $\langle\widetilde{z}\rangle \approx 0.25$ in model MLe1). This causes the stabilisation point to slightly move radially outwards (leaner conditions and lower progress variable) where the lower jet velocities allows the flame to move upstream. Overall, the main effect of including differential diffusion in the thermochemical database is to reduce the reaction rates, in particular for lean states in the mixture fraction space, which for the flame investigated leads to lower temperature gradients as compared to the case without differential diffusion.

The differences observed between models $\mathrm{M1}_{\mathrm{RES}}$ and $\mathrm{M1}_{\mathrm{TAB}}$ allow to investigate on the sensitivity of the source term $\dot{\omega}_z$ in Equation (13) to its implementation in the LES. When this source term is tabulated (model $\mathrm{M1}_{\mathrm{TAB}}$), the flame is predicted to stabilise at $x \approx 11D$ (as compared to $x \approx 10D$ for model $\mathrm{M1}_{\mathrm{RES}}$), which is closer to what observed in the experiments and for model MLe1. As shown in Figure 11, both models $\mathrm{M1}_{\mathrm{TAB}}$ and $\mathrm{M1}_{\mathrm{RES}}$ predict a steeper increase of temperature along the centreline with respect to model M0, and in better agreement with the experiments up to $x \approx 25D$. However, both models underestimate the maximum temperature and the mixture fraction as compared to the experiments. Similar considerations apply for the radial temperature profiles in Figure 12. This behaviour is consistent with the reaction rate contours observed in Figure 10, where one can observe that both models $\mathrm{M1}_{\mathrm{RES}}$ and $\mathrm{M1}_{\mathrm{TAB}}$ predict a maximum reaction rate at the flame base about 25% higher than that predicted with model M0. It is interesting to notice that the strongest reaction rate for models $\mathrm{M1}_{\mathrm{RES}}$ and $\mathrm{M1}_{\mathrm{TAB}}$ are found for values of progress variable similar to that observed for model M0, but at slightly richer conditions. This can only be associated with the different distribution of mixture fraction due to the introduction of the source term, since the same thermochemical database is used for models M0, $\mathrm{M1}_{\mathrm{RES}}$ and $\mathrm{M1}_{\mathrm{TAB}}$. This results in a stronger mixing predicted by the latter two, which can be observed from the steeper decay of mixture fraction along the centreline

observed in Figure 11, and from the shorter jet core (see for example iso-line of mixture fraction at $\langle\widetilde{z}\rangle = 0.47$ in Figure 10). Overall, no significant differences are observed in the predictions from models $M1_{RES}$ and $M1_{TAB}$, except for the aforementioned lift-off height.

Final considerations are provided for model M2 of Table 4, which yields more significant differences with respect to the other models. In this case the flame stabilisation point is predicted significantly more upstream, at $x \approx 5D$, as compared to the other models, as can be observed in Figure 10. Nevertheless, a very good agreement in temperature and mixture fraction profiles, and their rms vlaues, is still observed for $x \geq 14D$, as observed in Figure 12. Similarly to what observed for models $M1_{RES}$ and $M1_{TAB}$, accounting for differential diffusion models at the resolved level leads to the prediction of steeper axial gradients of temperature Figure 11 as compared to model M0, where differential diffusion is only included through the thermochemical database. Furthermore, the flame predicted by model M2 presents a longer inner branch burning at rich conditions with respect to the that predicted by the other models, as can be seen from the average reaction rate contour plots in Figure 10. The peak value of reaction rate at the flame base for model M2 looks about the same of that predicted by models $M1_{RES}$ and $M1_{TAB}$, where only the mixture fraction transport equation is corrected. The more upstream flame stabilisation location predicted by model M2 must therefore be explained by the combined correction of progress variable and mixture fraction transport equations. Further investigations (not shown) in particular indicate that the correction in model M2 leads to a higher mixture fraction diffusive flux, which locally widens the range of mixture fraction values. Moreover, the increased progress variable diffusive flux modelled through the β_c gradient in Equation (16) enhances the transport of progress variables across the flame, from products to reactants, leading to the stabilisation of the flame more upstream. This aspect is better investigated through the scatter plot analysis in the next section. Further sensitivity to the model parameter can be found in Appendix 3.

5.3. *Flame burning states*

Scatter plots of temperature, reaction rate and progress variable as predicted by the five LES models of Table 4 are shown in mixture fraction space in Figure 13. The scatter plots are coloured by the axial distance from the nozzle exit, $x/D = 0$, in order to distinguish between different regions in the domain. Conditional means are further reported in Figure 14 for easiness of comparison between the various models. One can notice for all five models that equilibrium temperature is only reached at lean conditions (as also seen in experiments [36]). A peak temperature of 1600 K is predicted by model MLe1, consistently with the results described in Section 5.2 and in good agreement with experimental measurements [36]. The models M0, $M1_{RES}$, $M1_{TAB}$ and M2, including differential diffusion in the thermochemical database, predict lower temperature values than model MLe1, in particular near stoichiometry and at rich conditions, which results from the lower reaction rate peak values in the thermochemical database. Model M2 predicts overall higher temperature values at stoichiometry and on the rich side, $\tilde{z}$>0.47. Moreover, burning states are found for this case up to $\tilde{z} \approx 0.8$, which is a result of the more upstream stabilisation of the flame. This different behaviour for model M2 is a consequence of the corrected diffusion flux in the progress variable equation, which enhances the flux of the progress variable across the flame front, from the outside (products) to the core of the jet (reactants), leading to the corresponding higher values of progress variable near the rich flammability limits as compared to the other models (see scatter plots of progress variable). Note that the

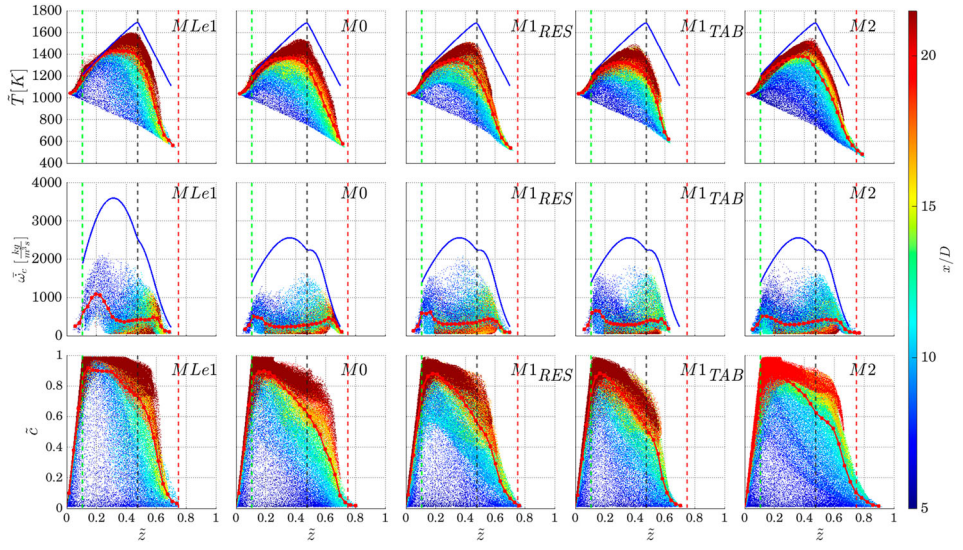

Figure 13. Scatter plots of temperature $\widetilde{T}$ (top), progress variable reaction rate $\bar{\dot{\omega}}_c$ (centre) and progress variable $\widetilde{c}$, (bottom) versus mixture fraction $\widetilde{z}$, coloured by the distance form the nozzle exit x/D. Only temperature values for $\widetilde{c}>0.1$ are shown to exclude unburnt conditions. Reaction rate values are only reported for the flame region, identified as the region where $0.1<\widetilde{c}<0.9$. Vertical dashed lines refer to the flammability limits and the stoichiometric condition. Conditional averages (−), equilibrium flamelets temperature (−) and maximum reaction rate in the flamelet database (−) are also shown.

correction term is non zero also outside the flammability range. Also, fully burnt states are not observed on the rich side for all models due to the fact that quick mixing in the inner, rich branch of the flame decreases the mixture fraction values as the reaction progresses.

Scatter plots of reaction rate are reported for $0.1<\tilde{c}<0.9$ and only show values higher than 2% of the maximum reaction rate in order to exclude points outside of the flame front. A bimodal behaviour is observed in the conditional mean of reaction rate where the two peaks identify respectively the lean premixed flame burning mode at the flame base ($x/D \approx 10$, blue colour) and the rich inner branch of the flame extending to an axial location of $x/D \approx 20$. The comparison between the conditional means of the models with (M0, $\mathrm{M1_{TAB}}$, $\mathrm{M1_{RES}}$, M2) and without (MLe1) differential diffusion (see Figure 14) reveals that the main difference in burning states is on the lean side, where the peak of the conditional mean is stronger and observed at higher values of $\widetilde{z}$ in the case without differential diffusion. On the contrary, the value and location of the peak on the rich side are similar between the cases with and without differential diffusion. This also indicates that the stronger effect on the flame-burning modes is given by the thermochemical database. In contrast, whether and how differential diffusion is taken into account at the resolved level seems to have a negligible effect on the lean side of the flame, while some influence is observed on the rich side. In particular, including correction in the resolved diffusive fluxes seems to overall move the peak of reaction rate in rich premixed mode towards leaner values, and this shift is less marked when corrections are applied to both fluxes of mixture fraction and progress variable (model M2). This might be due to the fact that model M2 predicts burning samples over a broader range of mixture fraction values on the rich side as compared to models $M1_{\mathrm{RES}}$ and $M1_{\mathrm{TAB}}$, as observed in Figure 14.

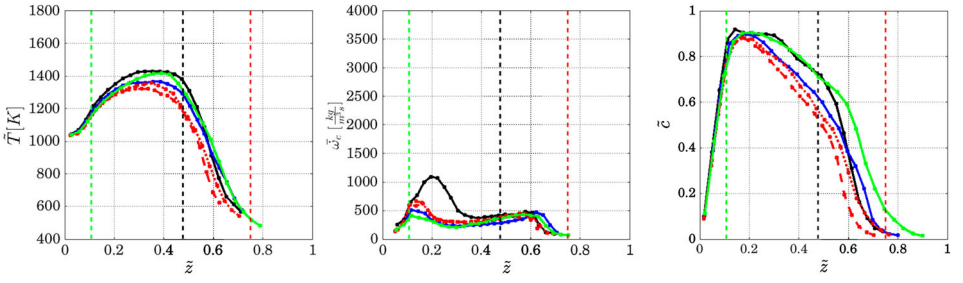

Figure 14. Conditional averages of temperature, reaction rate and progress variable in mixture fraction space, obtained from LES with models MLe1 (−), M0 (−), $M1_{RES}$ (···), $M1_{TAB}$ (− −) and M2 (−) of Table 4. Vertical dashed lines refer to the flammability limits and the stoichiometric condition.

6. Conclusions

Large eddy simulations of premixed and partially premixed turbulent hydrogen flames have been carried out in order to assess the relevance of differential diffusion models in the context of flamelet/presumed FDF combustion modelling. A turbulent fully premixed hydrogen flame in a slot burner configuration under thermo-diffusively unstable conditions was analysed first. Two models to account for differential diffusion at the resolved level were compared, where corrections to diffusive fluxes were applied respectively to the mixture fraction equation only and to jointly mixture fraction, progress variable and enthalpy equations. Results show that both models are capable of predicting the coupling between flame curvature and mixture fraction redistribution, leading to flame self-wrinkling and super-adiabatic temperatures. Despite the different formulations and implementation of the two models, they predict effects of similar entities in terms of superadiabatic temperature peaks and broadening of the mixture fraction range, suggesting that a correction on the mixture fraction field is sufficient for fully premixed cases without sources of enthalpy variation other than differential diffusion. A partially premixed lifted flame in vitiated coflow was simulated next. Four methods to account for differential diffusion models were compared between each other and against experimental data in their ability to predict the flame structure and the flame-burning states. Results indicate that the first and second-order statistics of temperature and mixture fraction are already in very good agreement with experimental measurements when differential diffusion is not taken into account either at resolved or at thermochemistry level, which is due to the fact that the lifted flame is strongly affected by the turbulent mixing ahead of the stabilisation point, that causes a predominant variation in the mixture fraction field as compared to differential diffusion. Therefore, the flame burns over the whole flammability range and conditions close to the flammability limits are reached. Including differential diffusion only at thermochemical level does not affect this mixing, but results in an overall reduction of the reaction rate and a consequent reduction of the temperature gradients. When the correction on the mixture fraction diffusion is included at the resolved level, the jet/coflow inert mixing appears mildly enhanced and an increase in the reaction rate at the flame base and temperature gradients is observed. When also the diffusion flux of the progress variable is corrected at resolved level, the increased diffusion flux of the progress variable from the products to the reactants causes an upstream shift of the flame stabilisation point as compared to the other tested models. How the correction in the mixture fraction diffusion flux is applied seems instead to have a negligible effect, quantifiable in a slight displacement of the flame

stabilisation point. An analysis of the burning modes reveals that the main effect of including differential diffusion in the thermochemistry is to lower the reaction rate peak on the lean branch of the flame and shift it towards leaner values. On the contrary, including differential diffusion at the resolved level seems to affect the rich branch of the flame and also to shift the reaction rate peak towards leaner values. As compared to the premixed flame, less sensitivity on the differential diffusion modelling is observed overall, which is a consequence of the strong aforementioned turbulent mixing ahead of the flame.

The models for differential diffusion assessed in the present study were originally derived for premixed cases, where relatively small mixture fraction variations around the nominal value and well within the flammability range are expected. The analysis conducted in the present work suggests that additional treatment might be necessary in partially-premixed cases where the mixture fraction spans values across the entire flammability range. This will be the focus of a future study.

Acknowledgments

The authors acknowledge the use of computational resources of the DelftBlue supercomputer, provided by Delft High Performance Computing Centre (https://www.tudelft.nl/dhpc). The authors also want to acknowledge their co-worker Alessandro Porcarelli for his contribution in the set up of the slot burner simulation.

Disclosure statement

No potential conflict of interest was reported by the author(s).

Funding

The authors acknowledge the Dutch Ministry of Economic Affairs and Climate (Ministerie van Economische Zaken en Klimaat) under the [TKI] scheme and Safran SA through the [APPU Project] for providing funding support to this work. The authors further acknowledge the use of the Dutch National Supercomputer Snellius [NWO project number 2021.043] and with the support of the SURF Cooperative using grant no. [EINF-8010] to perform the simulations reported in the present work.

References

[1] European Parliament and Council, *Directive 2014/94/eu of 22 october 2014 on the deployment of alternative fuels infrastructure (text with EEA relevance)*. Available at https://eur-lex.europa.eu/eli/dir/2014/94/oj.
[2] Y.B. Zeldvich, *The oxidation of nitrogen in combustion and explosions*, J. Acta Phys. -Chim. 21 (1946), p. 577.
[3] H. Pitsch, *A consistent level set formulation for large-eddy simulation of premixed turbulent combustion*, Combust. Flame 143 (2005), pp. 587–598.
[4] R.W. Bilger, S.H. Stårner, and R.J. Kee, *On reduced mechanism for methane-air combustion in nonpremixed flames*, Combust. Flame 80 (1990), pp. 135–149.
[5] J.D. Regele, E. Knudsen, H. Pitsch, and G. Blanquart, *A two-equation model for non-unity Lewis number differential diffusion in lean premixed laminar flames*, Combust. Flame 160 (2013), pp. 240–250.
[6] A. Porcarelli, B. Kruljević, and I. Langella, *Suppression of NOx emissions by intensive strain in lean premixed hydrogen flamelets*, Int. J. Hydrog. Energy 49 (2023), pp. 413–431.
[7] F.A. Williams, *Combustion Theory*, CRC Press, 2018.
[8] T. Poinsot and D. Veynante, *Theoretical and Numerical Combustion*, RT Edwards, Inc., 2005.
[9] A. Lipatnikov and J. Chomiak, *Molecular transport effects on turbulent flame propagation and structure*, Prog. Energy Combust. Sci. 31 (2005), pp. 1–73.

[10] M. Matalon, *Flame dynamics*, Proc. Combust. Inst. 32 (2009), pp. 57–82.
[11] P.E. Lapenna, L. Berger, F. Creta, and H. Pitsch, *Hydrogen laminar flames*, in *Hydrogen for Future Thermal Engines*, E.A. Tingas, ed., Springer International Publishing, Cham, 2023, pp. 93–139.
[12] L. Berger, K. Kleinheinz, A. Attili, and H. Pitsch, *Characteristic patterns of thermodiffusively unstable premixed lean hydrogen flames*, Proc. Combust. Inst. 37 (2019), pp. 1879–1886.
[13] M. Day, J. Bell, P. Bremer, V. Pascucci, V. Beckner, and M. Lijewski, *Turbulence effects on cellular burning structures in lean premixed hydrogen flames*, Combust. Flame 156 (2009), pp. 1035–1045.
[14] S.B. Pope, *Turbulent Flows*, Cambridge University Press, 2000.
[15] H. Pitsch, *Large-eddy simulation of turbulent combustion*, Annu. Rev. Fluid Mech. 38 (2006), pp. 453–482.
[16] D. Veynante and L. Vervisch, *Turbulent combustion modeling*, Prog. Energy Combust. Sci. 28 (2002), pp. 193–266.
[17] J. van Oijen and L. de Goey, *Modelling of premixed laminar flames using flamelet-generated manifold*, Combust. Sci. Tech. 161 (2000), pp. 113–137.
[18] M. Ihme, C.M. Cha, and H. Pitsch, *Prediction of local extinction and re-ignition effects in non-premixed turbulent combustion using a flamelet/progress variable approach*, Proc. Combust. Inst. 30 (2005), pp. 793–800.
[19] B. Fiorina, R. Vicquelin, P. Auzillon, N. Darabiha, O. Gicquel, and D. Veynante, *A filtered tabulated chemistry model for les of premixed combustion*, Combust. Flame 157 (2010), pp. 465–475.
[20] K. Bray, M. Champion, P. Libby, and N. Swaminathan, *Finite rate chemistry and presumed PDF models for premixed turbulent combustion*, Combust. Flame 146 (2006), pp. 665–673.
[21] A.N. Lipatnikov, V.A. Sabelnikov, F.E. Hernández-Pérez, W. Song, and H.G. Im, *A priori DNS study of applicability of flamelet concept to predicting mean concentrations of species in turbulent premixed flames at various karlovitz numbers*, Combust. Flame 222 (2020), pp. 370–382.
[22] J.F. Driscoll, J.H. Chen, A.W. Skiba, C.D. Carter, E.R. Hawkes, and H. Wang, *Premixed flames subjected to extreme turbulence: Some questions and recent answers*, Prog. Energy Combust. Sci. 49 (2020), pp. 189–208.
[23] A.C. Benim, B. Pfeiffelmann, P. Ocłoń, and J. Taler, *Computational investigation of a lifted hydrogen flame with LES and FGM*, Energy 173 (2019), pp. 1172–1181.
[24] Y. Xia, I. Verma, P. Nakod, R. Yadav, S. Orsino, and S. Li, *Numerical simulations of a lifted hydrogen jet flame using flamelet generated manifold approach*, J. Eng. Gas Turbine. Power 144 (2022), p. 091009.
[25] L. Berger, A. Attili, and H. Pitsch, *Synergistic interactions of thermodiffusive instabilities and turbulence in lean hydrogen flames*, Combust. Flame 244 (2022), p. 112254.
[26] M. Rieth, A. Gruber, F.A. Williams, and J.H. Chen, *Enhanced burning rates in hydrogen-enriched turbulent premixed flames by diffusion of molecular and atomic hydrogen*, Combust. Flame 239 (2022), p. 111740.
[27] M. Rieth, A. Gruber, and J.H. Chen, *The effect of pressure on lean premixed hydrogen-air flames*, Combust. Flame 250 (2023), p. 112514.
[28] J.A. de Swart, R.J. Bastiaans, J.A. van Oijen, L.P.H. de Goey, and R.S. Cant, *Inclusion of preferential diffusion in simulations of premixed combustion of hydrogen/methane mixtures with flamelet generated manifolds*, Flow Turbul. Combust. 85 (2010), pp. 473–511.
[29] A. Donini, R.J. Bastiaans, J.A. Van Oijen, and L.P. De Goey, *Differential diffusion effects inclusion with flamelet generated manifold for the modeling of stratified premixed cooled flames*, Proc. Combust. Inst. 35 (2015), pp. 831–837.
[30] N. Mukundakumar, D. Efimov, N. Beishuizen, and J. van Oijen, *A new preferential diffusion model applied to FGM simulations of hydrogen flames*, Combust. Theory Model. 25 (2021), pp. 1245–1267.
[31] H. Nicolai, L. Dressler, J. Janicka, and C. Hasse, *Assessing the importance of differential diffusion in stratified hydrogen–methane flames using extended flamelet tabulation approaches*, Phys. Fluids 34 (2022), p. 085118.

[32] R. Kai, T. Tokuoka, J. Nagao, A.L. Pillai, and R. Kurose, *Les flamelet modeling of hydrogen combustion considering preferential diffusion effect*, Int. J. Hydrog. Energy 48 (2023), pp. 11086–11101.
[33] Z.X. Chen, I. Langella, N. Swaminathan, M. Stöhr, W. Meier, and H. Kolla, *Large eddy simulation of a dual swirl gas turbine combustor: Flame/flow structures and stabilisation under thermoacoustically stable and unstable conditions*, Combust. Flame 203 (2019), pp. 279–300.
[34] Z.X. Chen, I. Langella, R.S. Barlow, and N. Swaminathan, *Prediction of local extinctions in piloted jet flames with inhomogeneous inlets using unstrained flamelets*, Combust. Flame 212 (2020), pp. 415–432.
[35] I. Langella, Z.X. Chen, N. Swaminathan, and S.K. Sadasivuni, *Large-eddy simulation of reacting flows in industrial gas turbine combustor*, J. Propuls. Power 34 (2018), pp. 1269–1284.
[36] R. Cabra, T. Myhrvold, J.Y. Chen, R.W. Dibble, A.N. Karpetis, and R.S. Barlow, *Simultaneous laser Raman-Rayleigh-LIF measurements and numerical modeling results of a lifted turbulent H_2/N_2 jet flame in a vitiated coflow*, Proc. Combust. Inst. 29 (2002), pp. 1881–1888.
[37] R. Cabra, J.Y. Chen, R.W. Dibble, A.N. Karpetis, and R.S. Barlow, *Lifted methane-air jet flames in a vitiated coflow*, Combust. Flame 143 (2005), pp. 491–506.
[38] R. Gordon, S. Starner, A. Masri, and R. Bilger, *Further characterisation of lifted hydrogen and methane flames issuing into a vitiated coflow*, in *Proceedings of the 5th Asia-Pacific Conference on Combustion*, 2005, pp. 333–336.
[39] Z. Wu, A.R. Masri, and R.W. Bilger, *An experimental investigation of the turbulence structure of a lifted H_2/N_2 jet flame in a vitiated co-flow*, Flow Turbul. Combust. 76 (2006), pp. 61–81.
[40] R.R. Cao, S.B. Pope, and A.R. Masri, *Turbulent lifted flames in a vitiated coflow investigated using joint PDF calculations*, Combust. Flame 142 (2005), pp. 438–453.
[41] W.P. Jones and S. Navarro-Martinez, *Large eddy simulation of autoignition with a subgrid probability density function method*, Combust. Flame 150 (2007), pp. 170–187.
[42] W. Han, V. Raman, and Z. Chen, *LES/PDF modeling of autoignition in a lifted turbulent flame: Analysis of flame sensitivity to differential diffusion and scalar mixing time-scale*, Combust. Flame 171 (2016), pp. 69–86.
[43] Y. Hu and R. Kurose, *Large-eddy simulation of turbulent autoigniting hydrogen lifted jet flame with a multi-regime flamelet approach*, Int. J. Hydrog. Energy 44 (2019), pp. 6313–6324.
[44] I. Langella, Z.X. Chen, N. Swaminathan, and S.K. Sadasivuni, *Large-eddy simulation of reacting flows in industrial gas turbine combustor*, J. Propul. Power 34 (2017), pp. 1269–1284.
[45] I. Langella and N. Swaminathan, *Unstrained and strained flamelets for LES of premixed combustion*, Combust. Theory Model. 20 (2016), pp. 410–440.
[46] A. Soli, I. Langella, and Z.X. Chen, *Analysis of flame front breaks appearing in les of inhomogeneous jet flames using flamelets*, Prog. Energy Combust. Sci. 49 (2021), pp. 189–208.
[47] J.A. van Oijen, A. Donini, R.J.M. Bastiaans, J.H.M. ten Thije Boonkkamp, and L.P.H. de Goey, *State-of-the-art in premixed combustion modeling using flamelet generated manifolds*, Prog. Energy Combust. Sci. 57 (2016), pp. 30–74.
[48] J.F. Driscoll, J.H. Chen, A.W. Skiba, C.D. Carter, E.R. Hawkes, and H. Wang, *Premixed flames subjected to extreme turbulence: Some questions and recent answers*, Prog. Energy Combust. Sci. 76 (2020), p. 100802.
[49] I. Langella, N. Swaminathan, and R.W. Pitz, *LES of turbulent premixed combustion behind a Bluff body*, in *9th Mediterranean Combustion Symposium*, June, Rhodes, Greece, 2015.
[50] K. Bray, P. Domingo, and L. Vervisch, *Role of the progress variable in models for partially premixed turbulent combustion*, Combust. Flame 141 (2005), pp. 431–437.
[51] I. Langella, N.A.K. Doan, N. Swaminathan, and S.B. Pope, *Study of subgrid-scale velocity models for reacting and nonreacting flows*, Phys. Rev. Fluids 3 (2018), p. 054602.
[52] Z.X. Chen, N.A.K.D. Doan, S. Ruan, I. Langella, and N. Swaminathan, *A priori investigation of subgrid correlation of mixture fraction and progress variable in partially premixed flames*, Combust. Theory Model. 22 (2018), pp. 862–882.
[53] T. Dunstan, Y. Minamoto, N. Chakraborty, and N. Swaminathan, *Scalar dissipation rate modelling for large eddy simulation of turbulent premixed flames*, Proc. Combust. Inst. 34 (2013), pp. 1193–1201.
[54] I. Langella, N. Swaminathan, Y. Gao, and N. Chakraborty, *Assessment of dynamic closure for premixed combustion large eddy simulation*, Combust. Theory Model. 19 (2015), pp. 628–656.

[55] G. Ferrante, Z.X. Chen and I. Langella, *Dynamic modelling of subgrid scalar dissipation rate in premixed and partially premixed flames with differential filter*,Appl. Therm. Eng. 248 (2024), pp. 123233). http://dx.doi.org/10.1016/j.applthermaleng.2024.123233.
[56] M.P. Burke, M. Chaos, Y. Ju, F.L. Dryer, and S.J. Klippenstein, *Comprehensive H_2/O_2 kinetic model for high-pressure combustion*, Int. J. Chem. Kinet. 44 (2012), pp. 444–474.
[57] J.O. Hirschfelder, C.F. Curtiss, and R.B. Bird, *Molecular Theory of Gases and Liquids*, John Wiley & Sons, New York, 1964.
[58] T.J. Poinsot and D. Veynante, *Theoretical and Numerical Combustion*, Edwards, 2005.
[59] S. Nambully, P. Domingo, V. Moureau, and L. Vervisch, *A filtered-laminar-flame PDF sub-grid scale closure for LES of premixed turbulent flames. Part I: Formalism and application to a bluff-body burner with differential diffusion*, Combust. Flame 161 (2014), pp. 1756–1774.
[60] *Chemical-kinetic mechanisms for combustion applications*, San Diego Mechanism web page, Mechanical and Aerospace Engineering (Combustion Research), University of California at San Diego; Available at http://combustion.ucsd.edu, last Accessed: 2023-10-06.
[61] A. Kazakov and M. Frenklach, *DRM 19, mechanism of elementary chemical reaction developped by the Gas Research Institute (GRI)*, preprint (1995). Available at http://combustion.berkeley.edu/drm/.
[62] J. Li, Z. Zhao, A. Kazakov, and F.L. Dryer, *An updated comprehensive kinetic model of hydrogen combustion*, Int. J. Chem. Kinet. 36 (2004), pp. 566–575.
[63] M. Ó Conaire, H.J. Curran, J.M. Simmie, W.J. Pitz, and C.K. Westbrook, *A comprehensive modeling study of hydrogen oxidation*, Int. J. Chem. Kinet. 36 (2004), pp. 603–622.
[64] R.I. Issa, *Solution of the implicitly discretised fluid flow equations by operator-splitting*, J. Comput. Phys. 62 (1986), pp. 40–65.
[65] Eindhoven University of Technology, *CHEM1D. A one dimensional laminar flame code*, preprint (2021).
[66] S.B. Pope, *Ten questions concerning the large-eddy simulation of turbulent flows*, New J. Phys. 6 (2004), p. 35.
[67] N. Kornev and E. Hassel, *Method of random spots for generation of synthetic inhomogeneous turbulent fields with prescribed autocorrelation functions*, Commun. Numer. Methods. Eng. 23 (2007), pp. 35–43.
[68] Y. Mizobuchi, J. Shinjo, S. Ogawa, and T. Takeno, *A numerical study on the formation of diffusion flame Islands in a turbulent hydrogen jet lifted flame*, Proc. Combust. Inst. 30 (2005), pp. 611–619.

Appendices

Appendix 1. Cabra flame: sensitivity to inlet turbulence

The Cabra flame, in particular its lift-off height, was observed to be very sensitive to the turbulent inlet conditions [40]. For this reason a preliminary analysis is carried out to ensure an accurate prediction of the jet spreading rate and its mixing with the coflow. Measured axial and radial rms velocity profiles, u' and v', reported in [40], are used as input parameters for the synthetic turbulence model [67] at the inlet. A sensitivity analysis on the imposed integral length scale ℓ_0 is carried out, together with an investigation of the effects caused by the velocity rms intensity on jet spreading and turbulent mixing. The imposed integral length scale is varied between 7% and 50% of the nozzle diameter D, and the rms intensity is varied from the measured value (characterized by a peak of 20% of jet bulk velocity) to 5% of this value. Mean temperature and mixture fraction centreline profiles are compared to experimental measurements [36] in Figure A1. The region upstream of the flame stabilisation location, $x \leq 10D$, is dominated by the mixing of the fuel stream with the coflow, which affects the distribution of mixture fraction and rms velocity and in turn the flame lift-off height. Results show that reducing velocity rms and integral length scale at the inlet causes a weaker jet spreading rate and a slower jet/coflow mixing. This results in a longer potential core, which is indicated by the less steep decay of the mixture fraction along the centreline. A similar effect of the rms intensity was observed in [40]. Nevertheless, the effect of inlet rms is observed to be mild as compared to that of the integral length scale at the inlet ℓ_0. For $\ell_0 = 0.5D$ in particular an overprediction of the mixing intensity is observed, resulting in the mixture fraction quickly falling within the flammability range and a consequent stabilisation of the flame significantly more upstream

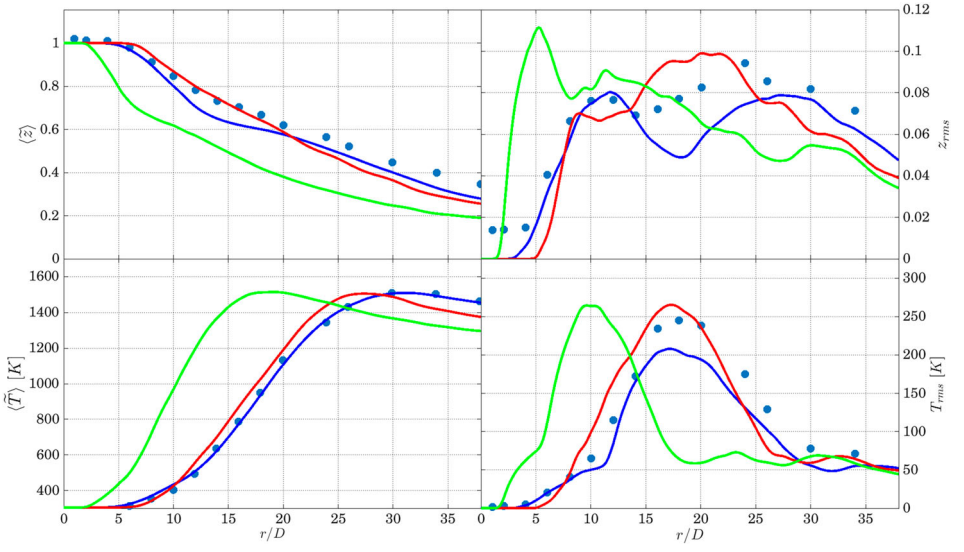

Figure A1. Centreline profiles of mean and rms temperature and mixture fraction. Symbols: experimental measurements from [36]. Lines: LES results obtained using the following conditions at the nozzle inlet: $\max(u_{\rm rms}) = 20$ m/s, $\ell_0 = 0.07D$ (–); $\max(u_{\rm rms}) = 20$ m/s, $\ell_0 = 0.5D$ (–); $\max(u_{\rm rms}) = 1$ m/s, $\ell_0 = 0.15D$ (–).

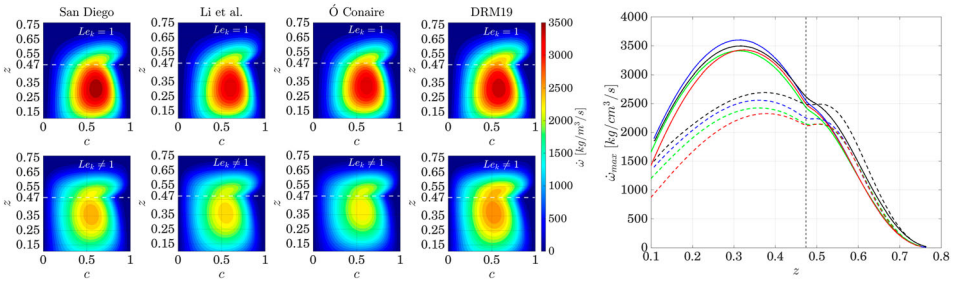

Figure A2. Left: contour plots of water-based scaled progress variable reaction rate in the $c - z$ space for a jet/coflow flamelet database with the reactant conditions reported in Table 2. Calculations obtained with unity Lewis number (top) and mixture averaged diffusion model (bottom), using different kinetic mechanisms. The stoichiometric condition $z_{\rm st} = 0.474$ is marked as a horizontal white dashed line Right: maximum reaction rate value versus mixture fraction from flamelet computations obtained using San Diego [60] (–), Ó Conaire [63] (–), Li et al. [62] (–) and DRM19 [61] (–) mechanisms. Solid and dashed lines refer respectively to the cases without and with differential diffusion. The stoichiometric condition $z_{\rm st} = 0.474$ is marked as a vertical black dashed line.

as compared to the experiments. A good match with the measurements is observed instead for $\ell_0 = 0.07D$. This condition is thus used for the simulations in the present study.

Appendix 2. Cabra flame: sensitivity to kinetic mechanism

A parametric analysis is performed here to investigate the effects of the chosen kinetic mechanism in the flamelet database on the flame lift-off height and the predicted statistics in the LES. Figure A2 shows the contour plots of the water-based scaled progress variable reaction rate in the progress variable and mixture fraction space resulting from 1D flamelets computation, as described in Section 3.3.

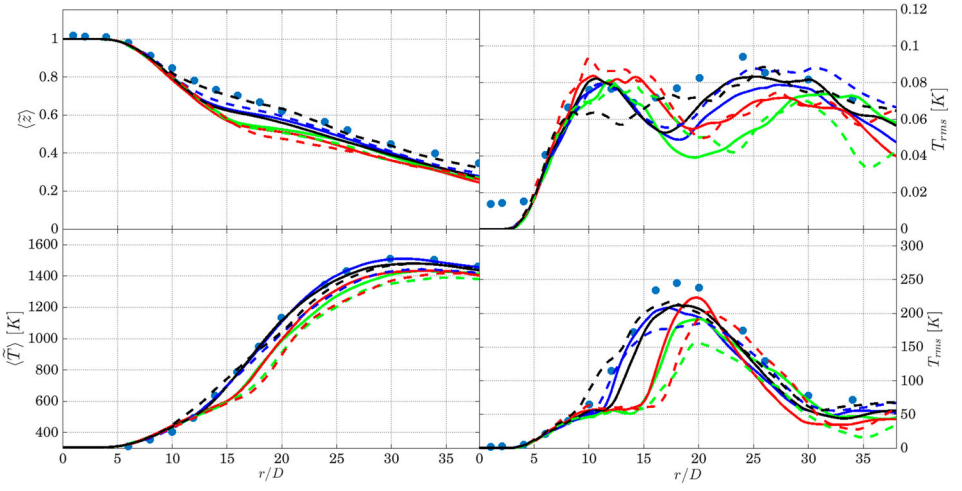

Figure A3. Centreline profiles of mean and rms temperature and mixture fraction. Symbols: experimental measurements from [36]. Lines: LES results obtained using San Diego [60] (−), Ó Conaire [63] (−), Li et al. [62] (−) and DRM19 [61] (−) mechanisms. Solid and dashed lines refer respectively to the cases without and with differential diffusion.

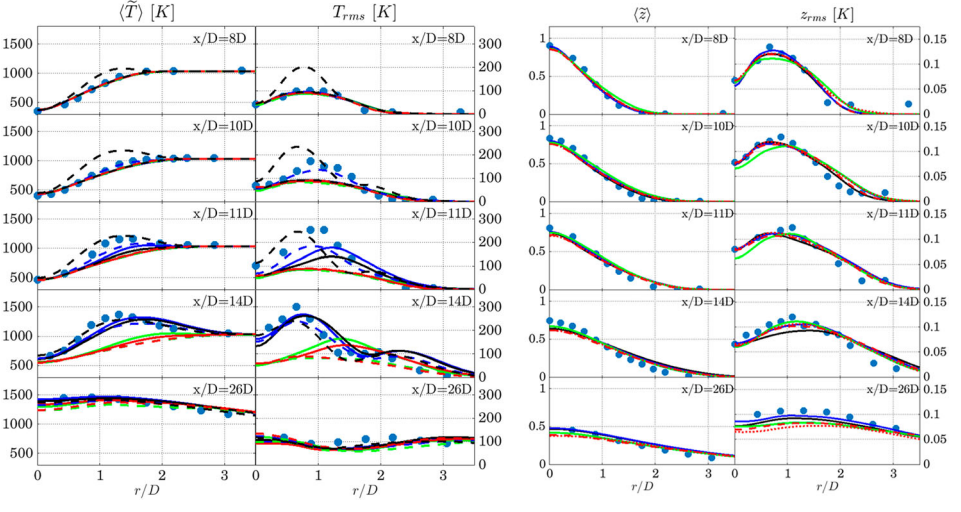

Figure A4. Radial profiles of time averaged and rms values of temperature and mixture fraction. Legend as for Figure A3.

The following kinetic mechanisms are compared: DRM19 [61], Li et al. [62], Ó Conaire [63], and San Diego [60]. The peak reaction rate value for each flamelet and from each mechanism is also plotted against the mixture fraction in Figure A2. When the assumption of species equidiffusivity is used, Li et al. and Ó Conaire mechanisms result in lower reaction rate peak values with respect to DRM19 and San Diego, and the peak location is found at slightly richer conditions than in the other two mechanisms. The San Diego mechanism gives the highest reaction rate values for the lean flamelets, followed by DRM19 that gives the highest values on the rich side. As compared to San Diego mechanism, Li et al. and Ó Conaire give similar values on the rich side and lower values for lean flamelets. When differential diffusion is included, the reaction rate values are observed to increase on the rich

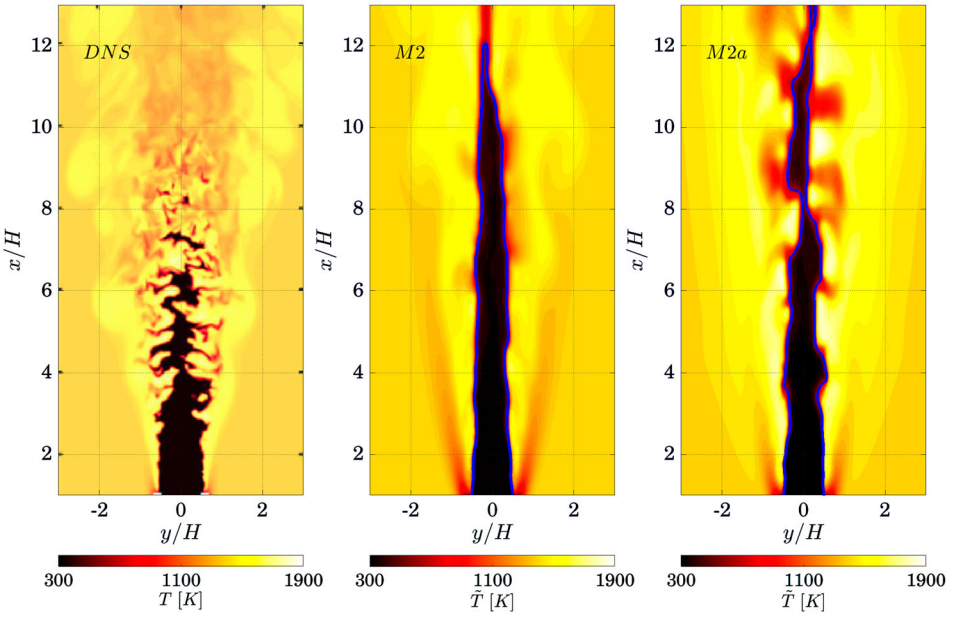

Figure A5. Midplane temperature contours from DNS [25] (left), LES M2 model of Table 3 (centre) and LES M2a case with increased β_z value in Equation (20) (right).

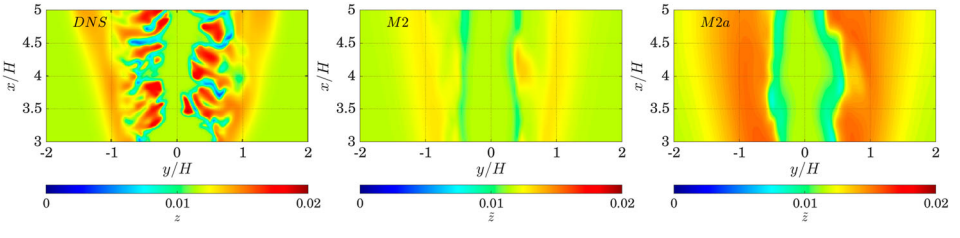

Figure A6. Midplane mixture fraction contours form DNS [25] (left), LES M2 model of Table 3 (centre) and LES M2a case with increased β_z value in Equation (20) (right).

side and decrease on the lean side as compared to the equidiffusivity case, with the peak shifting towards richer conditions. Also, the range in progress variable space with non-zero reaction rate is narrower for the lean flamelets and wider for the rich ones. Differences are further observed in the reaction rates predicted by the various mechanisms when differential diffusion is taken into account. In particular, the DRM19 mechanism yields a higher increase in maximum reaction rate on the rich flamelets when differential diffusion is included as compared to the other mechanisms. On the lean side, Li et al. and Ó Conaire mechanisms exhibit the weakest reaction rate.

The aforementioned differences in the flamelets database affect the flame characteristics in the LES. This can be appreciated by looking at the average and rms centreline temperature profiles in Figure A3. The lower reaction rates observed for Li et al. and Ó Conaire mechanisms in the unity-Lewis number case result in an overestimation of lift-off height (identified in the figure by the steep increase of centreline temperature) and consequently lower temperatures at downstream locations. San Diego and DRM19 yield instead similar predictions, with the former predicting the flame anchoring point slightly more upstream (see also radial average and rms temperature profiles in Figure A4). When differential diffusion is included in the database, different trends are observed for the various mechanism. San Diego and DRM19 mechanisms yield a more upstream prediction of the flame anchoring point (see Figures A3 and A4), which is due to the higher reaction rate at

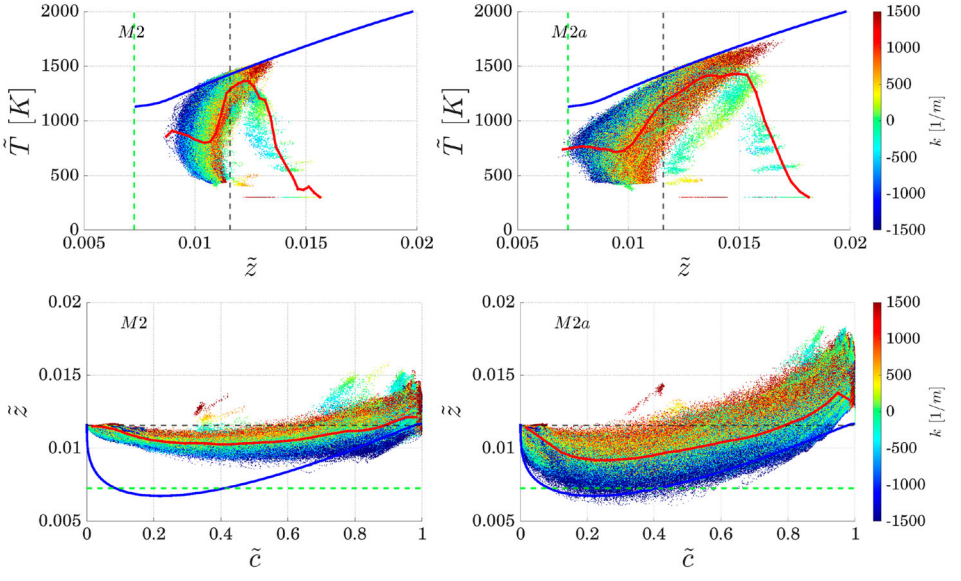

Figure A7. Scatter plots of filtered temperature versus filtered mixture fraction (top) and mixture fraction versus filtered progress variable (bottom) obtained from the LES of the premixed slot burner using LES model M2 of Table 3 (centre) and LES model M2a with increased β_z value in Equation (20) (right). Only values within the flame, identified using $0.1<\tilde{c}<0.9$, are considered. Lines as in Figure 9.

rich conditions observed for these mechanisms in Figure A2. An overprediction of the flame lift-off height with respect to the unity Lewis number case is observed instead when Li et al. and Ó Conaire mechanisms are used. This is due to the fact that these mechanisms yield the lowest reaction rate values for the lean flamelets. Overall, the San Diego mechanism is observed to yield the best match with experimental results and is therefore used in the present work for the analysis presented in the main text.

Appendix 3. Sensitivity to the differential diffusion model variables

The strategies to model differential diffusion at the resolved scales presented in the main text were originally developed for DNS of laminar flames. When applied to the LES framework, the filtering operation and the use of the presumed FDF can result in an attenuation of the correcting terms responsible for the controlling variables redistribution. These are the mixture fraction source term in models $M1_{RES}$ and $M1_{TAB}$, and the gradients of the parameters β_j in model M2. For this reason, a sensitivity analysis of model M2 is carried out by increasing the magnitude of parameter β_z in Equation (20) by a factor of four. This sensitivity analysis may also provide an overview of the expected trend associated with the use of a subgrid model for the differential diffusion/flame curvature interaction, imposing increased resolved diffusive fluxes. The case with increased β_z (renamed here as M2a to avoid confusion) is compared to the baseline case M2 of Table 3 discussed in the main text.

For the premixed flame, the increase in the mixture fraction diffusive flux correction leads to a significantly stronger development of thermodiffusive instabilities. As can be observed from the temperature contour plots in Figure A5, the flame front appears more wrinkled in case M2a as compared to case M2, with the formation of more pronounced cusps and occurrence of higher superadiabatic temperature peaks. Consistently, contour plots in Figure A6 show lower mixture fraction values upstream of the flame front for case M2a (increased value of β_z), and in the presence of cusps, as well as higher values of mixture fraction downstream of the flame front, in correspondence of convex

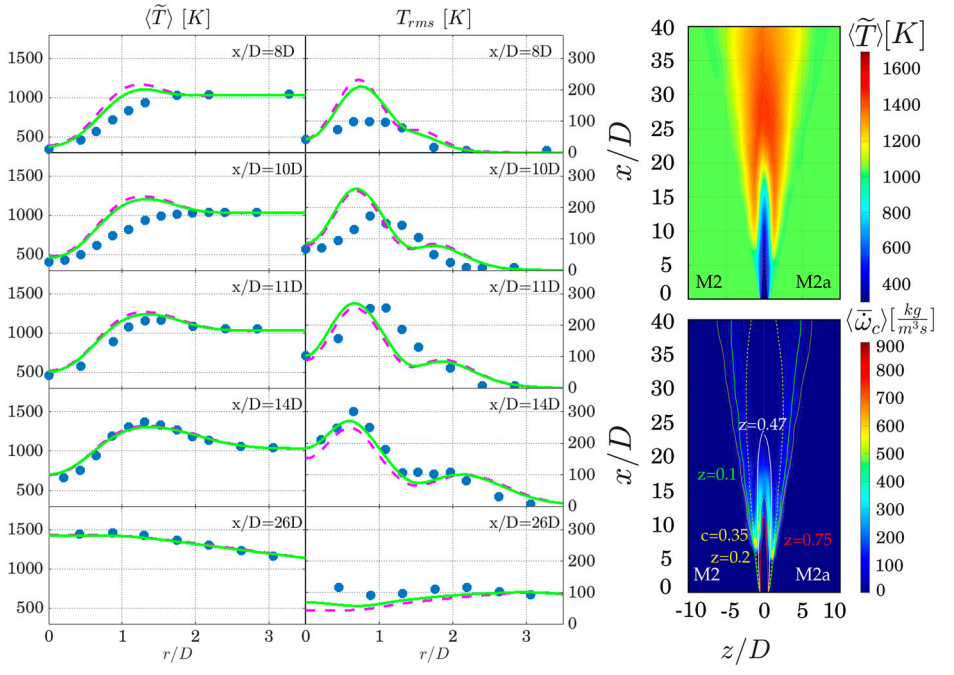

Figure A8. Left: Radial profiles of time-averaged and rms values of temperature. Symbols: measurements [36]. Lines: LES results with models M2 of Table 4 (−) and M2a case with increased β_z value in Equation (20) (−). Right: Mid-plane contours of time-averaged (top) temperature, and averaged filtered reaction rate (bottom) obtained from LES using the models M2 and M2a. Lines as in Figure 10.

flame front curvature towards the reactants. This leads to a broader range of mixture fraction values in closer agreement with the one observed in the DNS [25]. The comparison of the scatter plots in Figure A7 (bottom) confirms that the reciprocal interaction between the higher mixture fraction diffusive flux (caused by higher values of β_z) and increased flame wrinkling leads to a broader mixture fraction range in the burning states, as compared to the baseline case. In particular, model M2a shows overall leaner zero curvature burning states and all the mixture fraction values of the unstretched laminar flamelet (blue line) are reached, in correspondence with highly negative flame front curvatures. Moreover, model M2a predicts richer states associated with positive curvature throughout the progress variable range and in particular more towards the products $\tilde{c}$>0.5. The scatter plots of temperature (top row) show that richer reacting states predicted in case M2a are responsible for the higher aforementioned temperature peaks. The stronger mixture fraction diffusive flux couples with flame front curvature, enhancing the mechanism of flame wrinkling, as observable from the higher values of curvature magnitude.

The same analysis is repeated for the partially premixed lifted flame, although the sensitivity to the parameter β_z is milder than in the premixed case. The temperature and averaged reaction rate contour plots in Figure A8 show that a 4 times increment in β_z results in an upstream shift of the flame base of about $2D$. The same behaviour can be observed from the radial profiles in Figure right. This sensitivity highlights the relevance of the mixture fraction diffusive flux. In facts, even if turbulent mixing remains predominant for the studied lifted flame, an increased mixture fraction diffusive flux enhances the inert jet/coflow mixing upstream of the flame and can cause a significant redistribution of mixture fraction on the flame front, which in turns leads to an upstream prediction of the flame stabilisation point.